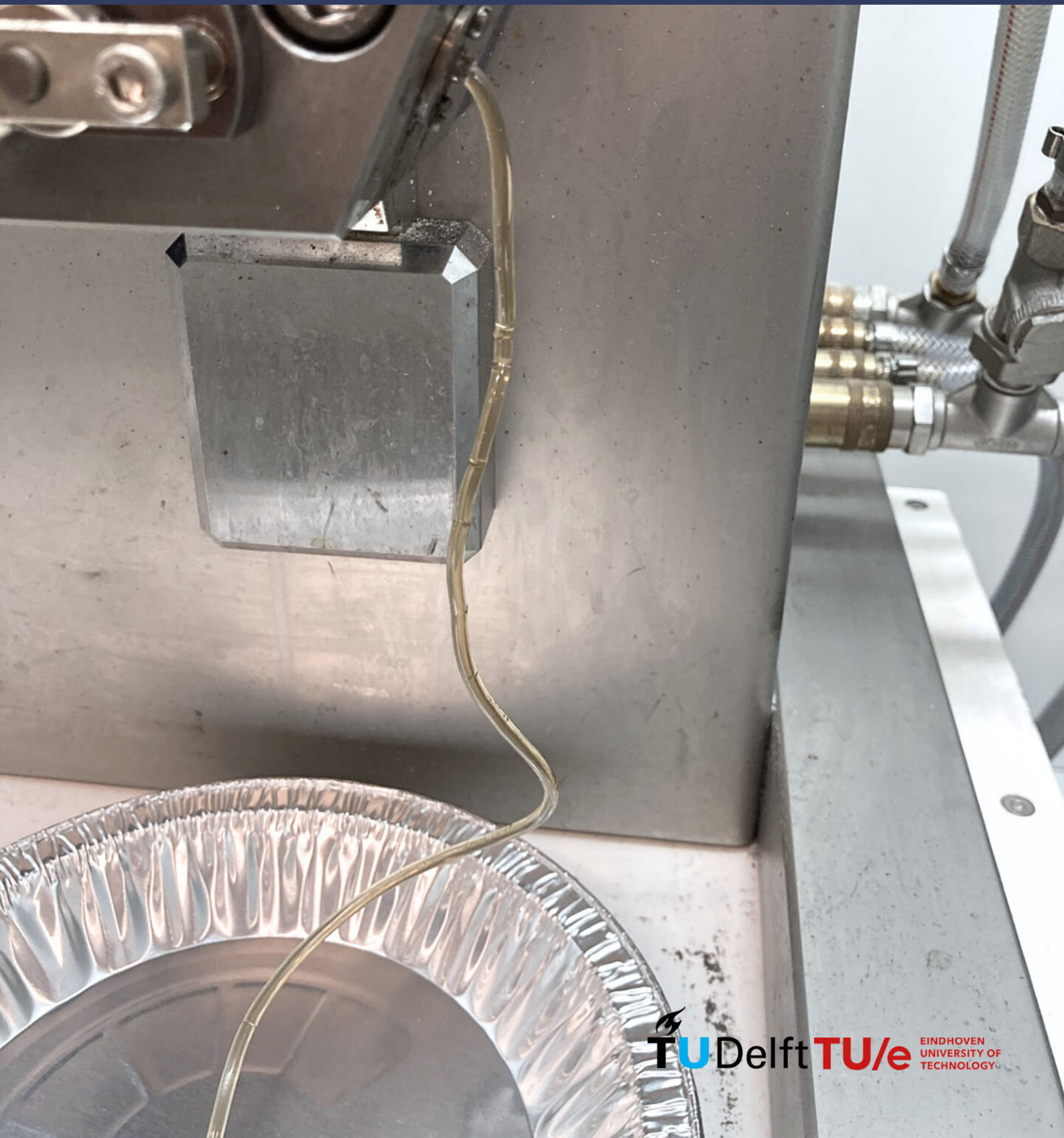# DESIGN OF PHOSPHATE-BASED DYNAMIC COVALENT NETWORK FOR FUSED DEPOSITION MODELING

Quentin Storm Cornelissen

Design of Phosphate-based Dynamic Covalent Network for Fused Deposition Modeling

by

Q.S. (QUENTIN) CORNELISSEN

Daily Supervisor

Prof. R.P. (Rint) Sijbesma   TU/e

Thesis Committee

Dr. S. (Sid) Kumar	TU Delft - Chair
Dr. G.A. (Georgy) Filonenko	TU Delft
Assoc. Prof. J.P.A.(Johan) Heuts	TU/e

Faculty of Mechanical, Maritime and Materials Engineering (3mE), TUDelft

Faculty of Chemical Engineering & Chemistry and Institute of Complex Molecular Systems, TU/e

June 15, 2023

Acknowledgements

Sid, I want to thank you for being my supervisor from TU Delft and Georgy for being in my thesis committee.

My parents, Lilian and Edwin, and my brother, Daniel, always supported me in everything what I do and I am lucky with such a supportive and incredible family. Hinke, I want to thank you for being there for me during moments of stress and worry, bringing me back to reality and providing support. I am really looking forward to our future together. A massive thanks to my roommates in Delft: Joost, Menno, Sem, and Wout. After long days in Eindhoven, it was always a pleasure to relax and have fun with all of you. Your friendship made the experience even more enjoyable.

Lastly, I would like to express my gratitude to my friends from my bachelor, my long-distance friends, and my friends who supported me throughout my Master's thesis. A special thanks goes to Raul, whom I had the pleasure of visiting in Paris during his master thesis.

Than you in advance for reading my Master thesis!

<div align="right">

Quentin Cornelissen
Delft, June 2023

</div>

Abstract

Additive manufacturing (AM) is considered an environmentally friendly manufacturing process that builds solid 3D structures layer-by-layer from a computer-aided design (CAD), resulting in reduced waste as opposed to conventional subtractive manufacturing. However, a significant challenge in AM is the extensive use of plastics, which lack a standardized recycling process. The insufficient adhesion between printed layers contributes to waste generated with AM. Therefore, it is important to prioritize sustainability as a design parameter for future AM materials.

Dynamic Covalent Networks (DCNs) offer a potential solution by combining the desirable characteristics of thermosets and the recyclability of thermoplastics. DCNs undergo bond rearrangement reactions influenced by external stimuli like heat or light, leading to changes in their topology. Bond exchange reactions can occur through two mechanisms: dissociative, involving separate steps of bond breaking and forming, or associative, involving simultaneous bond breaking and forming. Recently, a phosphate triester based DCN was developed obtaining a neighboring β-hydroxyl group which could perform transesterification exchange reactions within the network via the formation of a cyclic phosphate triester intermediate in a dissociative manner. Based on this network rearrangement, we synthesized a network by reacting phosphoric acid with a diglycidyl ether to perform ring-opening reactions which creates a pendent β-hydroxyl functional group assisted in neighboring group transesterification.

The reversibility of the bond exchange reaction within the network was investigated with a heating and cooling cycle with Variable temperature (VT) ^{31}P solid-state NMR (SSNMR). Furthermore, the network was reprocessable with compression molding at 130 °C. Fast relaxation times of 5 seconds at 200 °C were observed. Additionally, frequency sweep and dynamic mechanical temperature analysis (DMTA) experiments showed profiles which were expected for a dissociative bond exchange mechanism. However, an increase of the storage modulus at 150 °C was observed, indicating a curing process of the network. Subsequently, similar experiments were performed on the cured network, in which a reduction of the dynamic properties of the network was noted, with a stress relaxation time of 114 seconds at 200 °C. DMTA and frequency sweep experiments confirmed its increased storage modulus as well. Nevertheless, the uncured network was reprocessable via extrusion at 200 °C, however, it required at least 50 min for the network to obtain a viscous flow behavior for optimal extrusion.

Contents

List of Figures

List of Tables

1

Introduction

Additive manufacturing (AM) is a process of joining materials to build a 3D structure in a layer-upon-layer fashion. Whereas conventional subtractive manufacturing uses machining to remove material to produce the desired product. Producing products in a fast and consistent manner is the reason why this method of manufacturing remains the leading manufacturing technique at an industrial scale (Fig. 1.1).[1] AM has the freedom and flexibility to turn computer-aided designs (CAD) into complex 3D products in the biomedical, aerospace, automotive and packaging fields.[2] The layer-by-layer assembly, reduces the costs and time to design and produce molds or other tooling products. Furthermore, AM has less energy demand and reduces the production of scrap material as compared to subtractive manufacturing.[3]
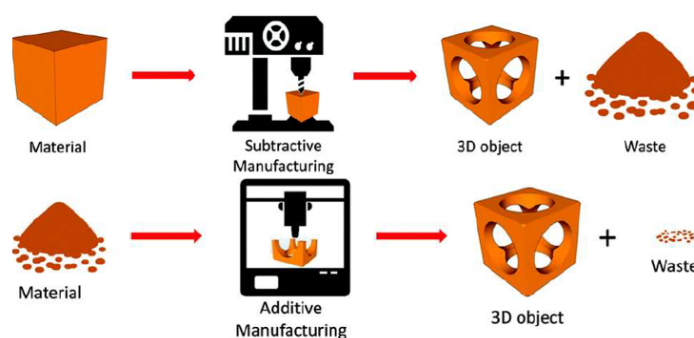
Figure 1.1: (Top) In subtractive manufacturing, a solid block of material undergoes machining processes to remove excess material until the desired 3D object is obtained. This approach often results in a significant amount of leftover scrap material. (Bottom) AM involves the layer-by-layer deposition of the necessary material, such as powder, liquid, or filament, to create the final 3D object. Compared to subtractive manufacturing, additive manufacturing generates substantially less waste material. Reproduced from [1].

Through the years, developments of various AM techniques, e.g. vat photopolymerization,[4] fused deposition modeling (FDM),[5] direct ink writing (DIW) [6] and selective laser

sintering (SLS) [7] promote more creativity in the use of different types of materials. Neverthe-less, 80.6 % of the global 3D printing materials revenue comes from polymers according to Wohlers Report of 2019.[8] Notwithstanding, the absence of a standardized recycling process for polymers, the polymer materials are generally incinerated or disposed of at a landfill.[9] In order to prioritize sustainability in polymeric materials for AM, it is necessary to decrease the production by engaging in reusing and recycling of polymeric materials.

The main problem with 3D printed products is poor adhesion between the printed layers, causing inconsistency in the printed products, leading to much polymer waste (Fig. 1.2). [2, 10, 11]

Vertical Forces   Horizontal Forces
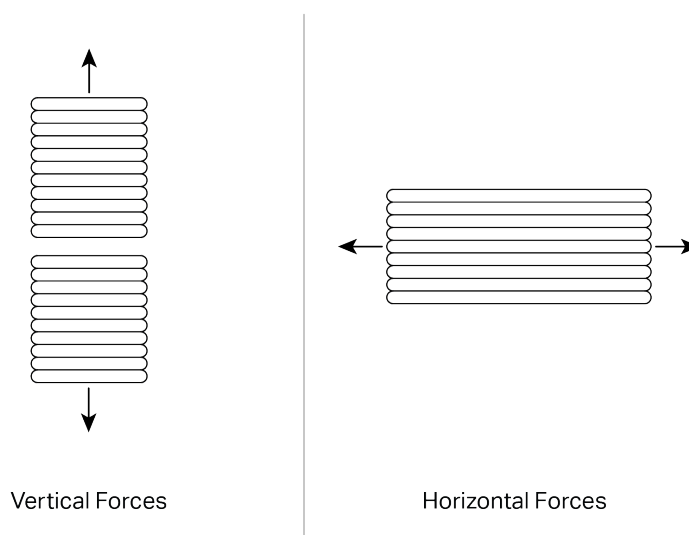
Figure 1.2: Illustrations of printed layers show strength in tension parallel to the layers. While the printed layers exhibit weakness when subjected to tension perpendicular to the layers. Reproduced from [12].

Recently, the use of Dynamic Covalent Networks (DCNs) within AM has attracted attention, due to its potential in providing a practical solution to the current problems.[2, 13–15] DCNs combine the mechanical benefits of a traditional thermoset with the shape changing response to external stimuli found in thermoplastic materials. This is achieved through reversible bond exchange reactions within the polymer's crosslinking strands, which occur upon the application of a stimulus such as heat or UV. DCNs provide self-healing, shape-memory, reprocessable and recyclable characteristics.[16]

Two types of DCNs based on their reaction mechanism are available, dissociative and associative. The former means that breaking and rebuilding of chemical bonds take place consecutively.[16] For the latter, the mechanism of bond breaking and reforming occurs simultaneously (Fig. 1.3). The main difference is the practically fixed crosslink density of associative DCNs, i.e. vitrimers, in contrast to dissociative DCNs in which the crosslink density temporarily decreases during bond exchange reactions.[16]
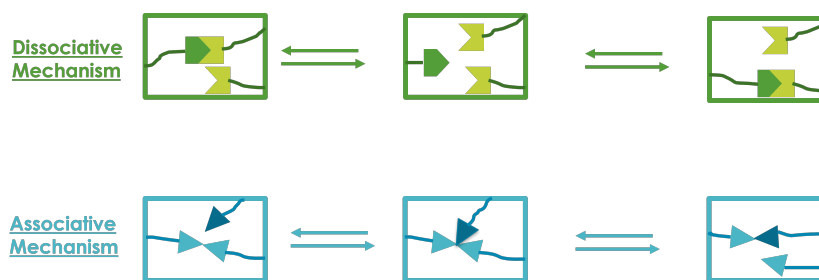
Figure 1.3: (Top) Dissociative bond exchange mechanism, whereby bond breaking and forming occurs in two seperate steps, which temporally decreases the crosslink density. (Bottom) Associative bond exchange mechanism, where bond breaking and forming occurs simultaneously. Redrawn from [16].

In 1966, Craven developed one of the earliest known DCNs in the laboratories of DuPont. This network was based on a Diels-Alder (DA) and retro DA reaction.[17] Expanding on this, DA chemistry was subsequently utilized to synthesize polymeric materials. Notably, in 2002, Wudl and colleagues reported a polymeric network with thermally repairable abilities exclusively based on DA covalent bonds.[18]

Fast forward to the present, numerous amounts of chemistries have been developed to synthesize DCNs. Figure 1.4 below provides a summary of both dissociative and associative covalent bond exchange chemistries.
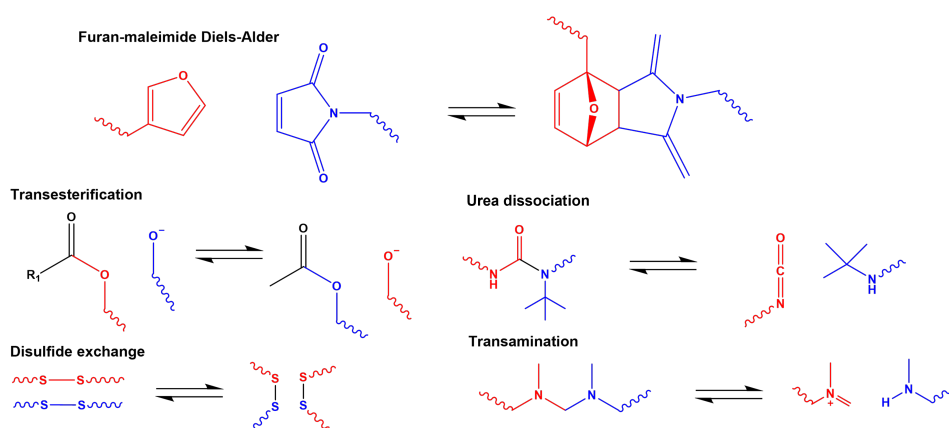
Figure 1.4: Several bond exchange chemistries found in literature. Reproduced from [19].

The aim of this study is to develop a dynamic covalent network which is printable with fused deposition modeling. In order to obtain it, a state of the art of dynamic covalent networks in additive manufacturing is discussed. Subsequently, an approach of the experimental work is outlined, in which the chemistry behind the material and the methods of characterizing are explained. Furthermore, the results of the research will be discussed, by showing predominantly stress relaxation and dynamic mechanical temperature analysis experiments to understand the dynamicity and mechanical behavior under various temperatures. At last, results are shown whether the network is extrudable.

2

Theoretical Background

This chapter will commence by explaining in short the workings of a fused deposition modeling (FDM) printer; which material parameters are important to consider and why dynamic covalent networks (DCNs) can improve the production of printed parts. Subsequently, the state of the art of DCNs for FDM and other additive manufacturing (AM) techniques is provided.

2.1   Fused deposition modeling

Fused Deposition Modeling (FDM) is among all 3D printing techniques the most user friendly and popular for scientists and hobbyists.[20–22] It is an extrusion-based technology whereby solid polymer filament is heated to a molten state to create a material that can flow. Once the polymer flows and arrives at the nozzle, the material transforms into a viscoelastic state and is extruded out of the nozzle where it is deposited as roads or extrudates on a XY-plane (Fig. 2.1). After extrusion, the viscoelastic material solidifies and fuses together for better adhesion, and is eventually cured into a solid 3D structure. This process is very similar to the conventional method of extrusion; injection molding.
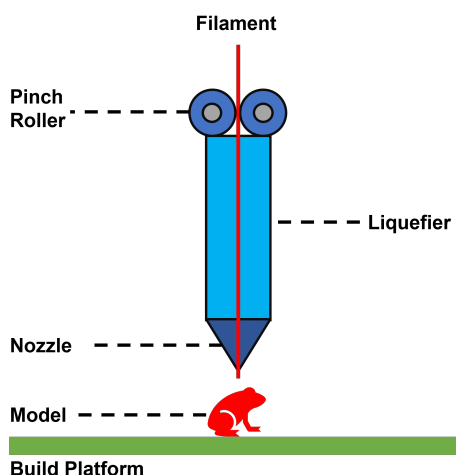
Figure 2.1: Schematic of a FDM printer. Redrawn from [23].

To design a filament for FDM, several material parameters have to be considered, such as the glass transition temperature (T_g), which characterizes the material transition from a rigid, glassy state to a more flexible, rubbery state. Additionally, the flow activation energy (E_a) describes the energy required in order for the material to flow, while the viscosity (η) influences the ease with which the material flows at a given temperature. Moreover, both the viscosity and the ratio of the loss modulus (G'' or E'') and storage modulus(G' or E'), tan(δ), should not be too high, otherwise more pressure is required to extrude the material out of the nozzle. Finally, the thermal expansion must be taken into account, as it can cause anisotropy on the final product, ultimately affecting the final quality of the printed object.

Currently, amorphous thermoplastics are more favored, as opposed to semi-crystalline materials, due to the lower thermal expansion coefficient and enhanced polymer chain diffusion. In contrast, semi-crystalline materials crystallize upon cooling, resulting in less layer adhesion. However, semi-crystalline polymers generally offer more toughness and obtain a higher surface temperature.[24, 25] Commonly varieties of thermoplastic polymers used are acrylonitrile butadiene styrene (ABS), polycarbonate (PC), polylactic acid (PLA) and polyamide (PA).[26]

2.2 Development of additive manufacturing with dynamic covalent networks

2.2.1 Fused deposition modeling

The earliest study found on printing DCNs with FDM was in 2016, performed by Davidson *et al.*[27] who designed a printable DCN with commercially available PLA containing a furan-maleimide Diels-Alder (fm-DA). Davidson *et al.* printed dog-bone shapes with three different infill patterns and compared the mechanical strengths of PLA containing DCNs to neat PLA. The two linear patterns parallel and perpendicular to the direction of the mechanical stress showed higher strength and toughness with increasing concentration of dynamic bonds. The presence of DCNs within the material allows for the formation of new covalent bonds between interfilamentous junctions, resulting in a homogeneous cross section (Fig. 2.2).
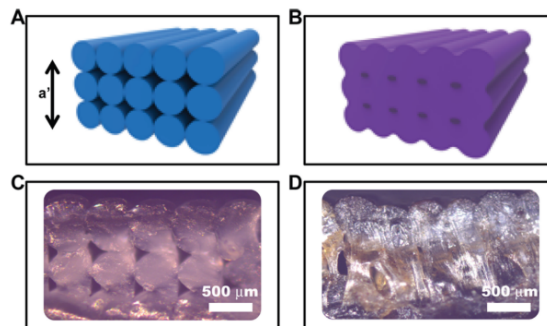
Figure 2.2: (A) Illustration of 3D-printed PLA filaments, (a') is the interfilament junction. (B) Illustration of the dynamic PLA. (C) Microscopic image of printed neat PLA filaments. (D) Microscopic image of 3D printed dynamic PLA. Reproduced from [27].

Subsequent work from the same group and Yang *et al.*[28] printed a similar fm-DA based DCN and investigated more properties. Their material achieved a recovery of strength of 77 % after only healing for 15 min at 65 °C.[14] Furthermore, Yang observed a reduction of the roughness for their DCNs compared to similar polyurethane conventional printing filaments, with a roughness reduction of at least 67 % (Fig. 2.3). Likewise, the anisotropy was between 0.6 and 4 %, whereas the polyurethane conventional filaments exhibited a minimum anisotropy of 50 %. The results confirm the significant improvement of adhesion and surface roughness by printing with DCNs.
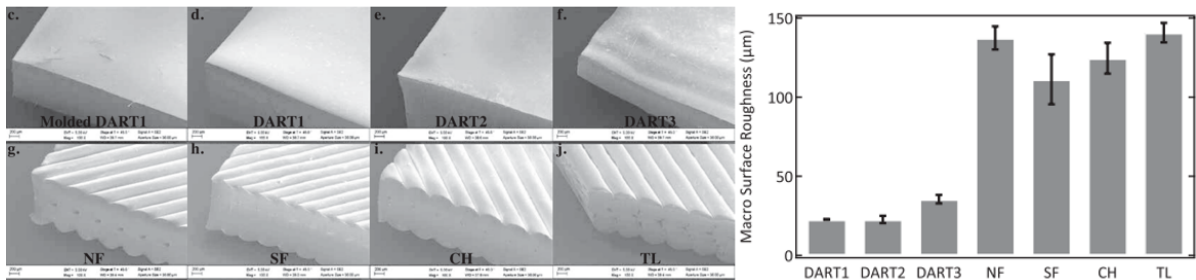
Figure 2.3: SEM images of the surface morphologies of printed fm-DA filament, in which DART1, 2 and 3 are different concentrations of crosslinker, (left figure, top row) and of conventional polyurethane thermoplastic filaments (left figure, bottom row). The right figure represents the total difference in surface height of each printed filament. Reproduced from [28].

Further, Kim *et al.*[29] provided a comprehensive study on upcycling ABS into a recyclable ABS-vitrimer. It exhibited a higher mechanical performance with around 1.6 times higher strength than neat ABS, due to the enhanced interlayer integration. The dynamic imine exchange reaction within the DCN also had a high E_a of approximately 151 kJ/mol. Kim states that a high E_a ensures stability at lower temperatures near T_g and faster bond exchange upon heating, which is optimal for 3D printing with a DCN. Moreover, the remarkable attribute of this ABS-vitrimer is the ability to mix with any waste of neat-ABS, ABS-vitrimer or unsorted mixtures produced during manufacturing and upcycle it by 3D printing again. However, the recyclability of the vitrimer may reach a limit, leading to the weakening of its mechanical performance due to side reactions at elevated temperatures.

In another study, performed by Niu *et al.*,[30] side reactions also seem to detriment the recyclability. Niu printed a polyurea vitrimer repeatedly and found a decrease in Young's modulus of 19 % after the fifth cycle. Nonetheless, the ability to recycle this polymer material up to five cycles is a great improvement, in contrast to conventional polymeric materials.

Additionally, DCNs could also be used for 4D printing, whereby a DCN can exhibit shape-memory abilities upon exposure to a stimulus. Joe *et al.*[31] and Choi *et al.*[32] both developed a DCN based on transesterification reactions. Joe *et al.* investigated the influence of different concentrations of catalyst present in the material and found that the stress relaxation and bond exchange times decreased with increasing concentration. Simultaneously, the crystallinity

reduced and the chance of faster degradation of the catalyst enhanced. A balance between stability of the final product and faster healing times is important in order to print a DCN.

To test the shape-memory behavior of the material, a bridge made of polycaprolactone-vitrimer was printed. The bridge featured conductive silver paste positioned underneath, with a small light bulb placed on each side. Once heat was applied, the bridge closed and current flowed through to each side to turn the light bulbs on, confirming its shape changing ability (Fig. 2.4c). Furthermore, Choi *et al.* welded PLA paddles to a printed ship using an epoxy vitrimer, in which the paddles change shape at 40 °C and restore once cooled down. The interfacial welding between PLA and the vitrimer was enabled by the presence of ester groups in PLA, which could react with the epoxy groups of the vitrimer (Fig. 2.4a).

Finally, this approach of multi-material printing can potentially be used for soft robotic applications. Roels *et al.*[33] performed a comprehensive study on AM of elastomeric DA networks for soft robots. Soft robots are prone to tearing and piercing and therefore, could benefit from self-healing materials. Roels printed grabbers that could grab different objects while having the ability to self-heal and completely recover from large cuts (Fig. 2.4b).
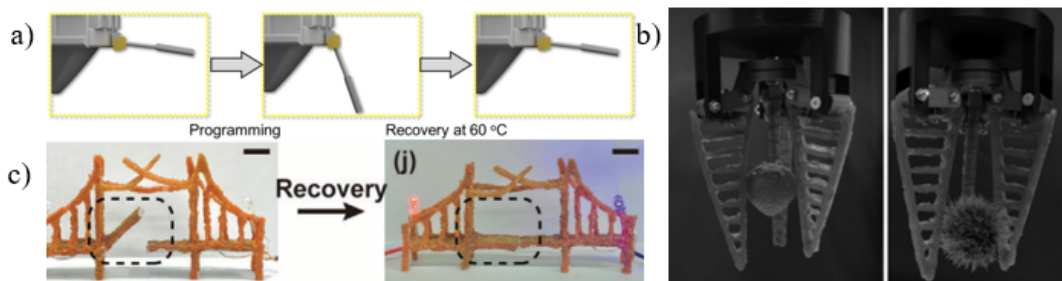
Figure 2.4: a) A printed paddle could easily be welded with an epoxy vitrimer, and had the ability to bend when heated to 60 °C. Reproduced from [32]. b) A grabber that was printed with an elastomeric DA network for soft robots. Reproduced from [33]. c) The printed bridge platform demonstrates shape memory behavior when subjected to heating. Reproduced from [31].

2.2.2 Direct ink writing

Direct Ink Writing (DIW) is an AM technique similar to FDM, however, the main difference is that FDM melts a solid filament material in order to extrude, and DIW extrudes a shear-thinning polymeric ink. Consequently, incorporating additives within the polymeric ink is simply done, thereby enhancing abilities within the material and improving its characteristics. For instance, Shi *et al.*[13] performed a study, which is the most referred study on 3D printing with DCNs, whereby a recyclable vitrimer epoxy ink mixed with nanoclays was printed multiple times to confirm its recyclability. The nanoclays were added to increase the viscosity and to strengthen the material to maintain shape after extrusion. The comprehensive production and recycling procedure involved many steps and long curing times, however, it is a first proof of concept (Fig. 2.5).
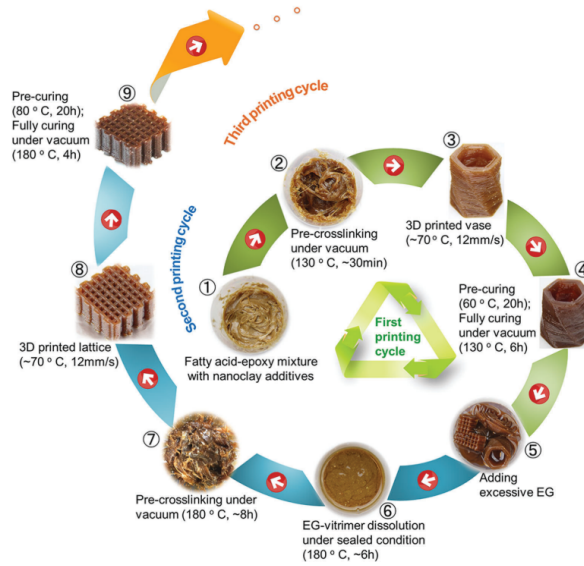
Figure 2.5: The production and recycling cycle of nanoclay-reinforced vitrimer epoxy through DIW
was developed. Reproduced from [13].

DIW offers the advantage to easily include additives within the ink to obtain enhanced
abilities within the material, as demonstrated by Zheng *et al.*[34]. In their work, hydroxylated
multi-walled carbon nanotubes were mixed with the DCN, enabling localized healing of the
material using light without the need to unnecessarily heal the entire object. Locally healing
specific parts on the printed object opens up more possibilities in extending the life-time of the
printout. The printouts showed a reduction of the interfilament junctions on micro scale and
better adhesion between the layers. Additionally, a near infrared laser could target areas and
locally decrease the viscosity, which has the benefit of removing support structure easier (Fig.
2.6).

Figure 2.6: Support structures can be precisely removed by locally applying laser induced heat.
Reproduced from [34].

2.2.3 Selective laser sintering

Selective laser sintering (SLS) fuses polymeric particles together in a layer-by-layer fashion,
whereby similar issues as observed in extrusion-based AM techniques are encountered. Sun *et
al.*[35] designed two polyurethane materials containing dynamic halogenated bonds, whereby

improved tensile strength was observed in the Y-, and Z-axis. The tensile strength in the Z-direction was around 88 % of that in the X-axis strength, which surpasses the performance of a similar commercially available thermoplastic polyurethane (TPU) powder, exhibiting only 59 % of the X-axis strength (Fig. 2.7a). Evidently, the adhesion of the sintered particles improved significantly with DCNs.

At last, Sun *et al.*[36] investigated SLS printing of a DCN based on dynamic urea bonds, and printed an orthotic insole including a porous structure, which was damaged and completely healed after heating it for 1 hour at 120 °C (Fig. 2.7).
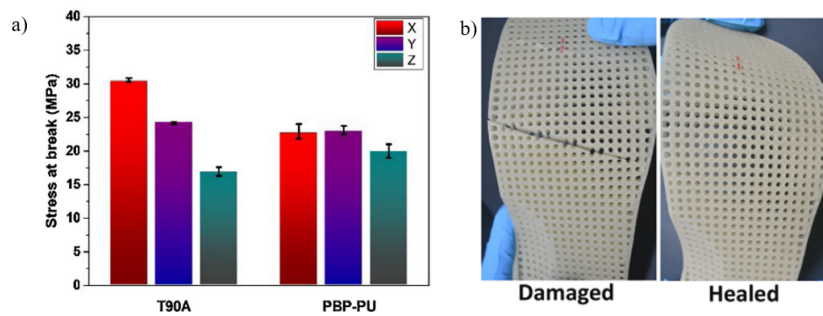
Figure 2.7: a) Tensile strength of printed commercially available thermoplastic polyurethane (TPU), named T90A, and polyurethane-based DCN samples in the X-, Y-, Z-direction. Reproduced from [35]. b) A printed orthotic insole with a DCN based on dynamic urea bonds demonstrated the ability to undergo damage and subsequent self-healing after heating. Reproduced from [36].

2.2.4 Vat photopolymerization

Vat photopolymerization techniques, such as stereolithography (SLA) and digital light processing (DLP), operate on the principle of chemically transforming photoinitiators present in a liquid resin vat. Upon exposure to light, these initiators start to react with liquid monomers and oligomers. A 3D object is eventually formed layer-by-layer, and can be taken out of the liquid resin. SLA and DLP show numerous examples of high resolution printed DCNs with self-healing capabilities. Examples are presented in Figure 2.8, whereby Robinson *et al.*[37], Zhang *et al*[38] and Cui *et al.*[39] all designed materials that can change shape under a stimulus. A practical example can be seen in Figure 2.8b, in which Cui *et al.* designed a toy grabber which could grab and unload weights.
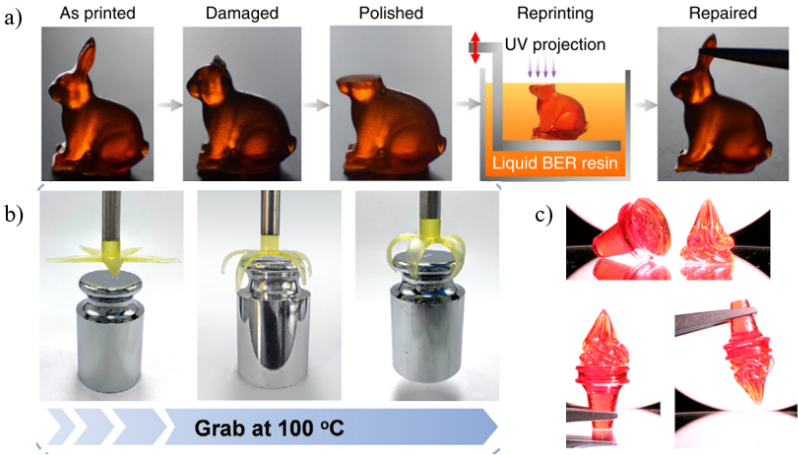
Figure 2.8: a) A rabbit was printed with DLP, which was damaged and repaired again. Reproduced from [38]. b) At 100 °C, the shape memory behavior allowed for the grabbing and lifting of a 500 g weight. Reproduced from [39]. c) A printed ice cream cone and ice cream were welded together after being subjected to a temperature of 65 °C for 16 hours. Reproduced from [37].

3

Approach

Having obtained more insights from the previous studies, the objective of this chapter is to delve into the chemistry behind the designed dynamic covalent network (DCN). Furthermore, the selected materials are discussed, followed by a comprehensive overview of the characterization methods employed in the study.

3.1 Chemistry

Neighboring group participation

The chemistry of the ultimately designed network is based on transesterification, which is a well-known chemistry that usually occurs at elevated temperatures and the presence of a catalyst. The principle is a reaction between an ester and a free alcohol group yielding a new ester and alcohol. Generally, transesterification reactions result in shuffling of the moieties (Fig. 1.4). Unfortunately, utilizing catalysts has the problem of eventually leaching out, which may reduce the dynamic properties of the materials over time and can be harmful to the environment.[40] A self-catalyzed system would overcome these issues, and the goal of this work is to develop such a system. An example of neighboring group participation is implemented by Zhang *et al.*[41, 42] in which carboxylic groups can react upon heating with the pendent neighboring ester group (Fig. 3.1).
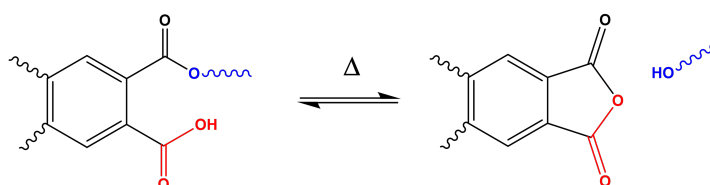
Figure 3.1: Transesterification reaction of neighboring carboxylic acid groups. Redrawn from [41].

Phosphate chemistry

With this in mind, in 2021, Majumdar *et al.*[43] introduced a phosphate triester based DCN that can perform transesterification at elevated temperature using neighboring group participation as well. The network consist of phosphate triesters, in which two arms are polymer chains of trifunctioncal polycaprolactone (PCL) and one reacted with ethylene glycol. Once heated, the β-hydroxyl group within that chain can attack the phosphate, and the dissociated cyclic triester intermediate is formed whereby a PCL chain is removed. Upon cooling, the system can turn back into the associated linear state, in which the free -OH group from the chain can attack the phosphate again (Fig. 3.2). This network showed fast relaxation times and was able to extrude at 120 °C.
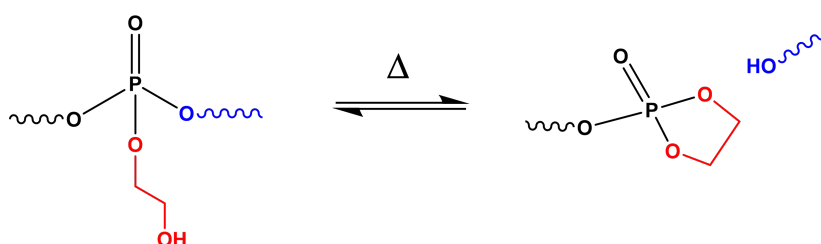
Figure 3.2: Transesterification of the pendent β-hydroxyl group, leading to the removal of the PCL chain. Redrawn from [43].

Reaction of phosphoric acid with a diglycidyl ether

Another approach of neighboring group participation involves the reaction of phosphoric acid (A_3) with a diglycidyl ether (B_2) to perform a ring-opening reaction of the epoxide, creating a pendent β-hydroxyl group.[44] The reaction is an epoxide ring opening reaction in which the free electrons of the P-OH group attacks, at random, the α or β C-atom of the epoxide (Fig. 3.3).[45]
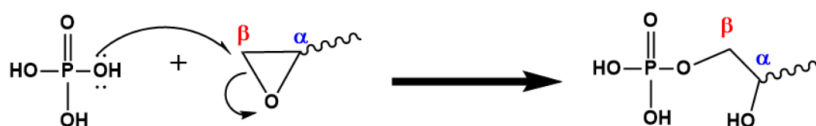
Figure 3.3: Reaction mechanism of phosphoric acid reacting with an epoxide. Only the attack on the β is drawn. Redrawn from [45].

Through the reaction of the diglycidyl ether and phosphoric acid in a 1:1 ratio, the reaction stops upon complete consumption of the P-OH groups, leading to the formation of a mixture of phosphate mono-, di- and triesters. This formation of epoxy resins including phosphates esters can be applied to coatings to provide flame retardancy within the resin.[46, 47] In addition, phosphate esters can provide biodegradable [48, 49] and antifouling [50] properties into the material.

Accordingly, the formation of phosphate di- and triesters provides dynamic properties by

performing bond exchange reactions similar to the chemistry of Majumdar's network, but with a pendent β-hydroxyl group within each chain (Fig. 3.4).
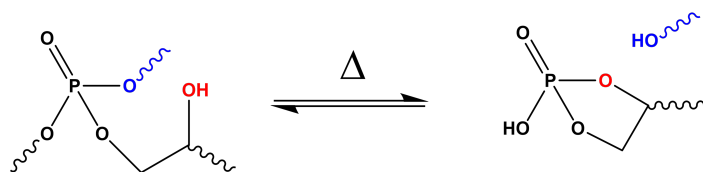
Figure 3.4: Bond rearrangement reaction of phosphate triesters, after reacting phosphoric acid with an epoxide.

The chosen diglycidyl ether for the developed network is bisphenol-A propoxylate diglycidyl ether (BAPDGE). It has a similar chemical structure to the most well-known epoxy resin bisphenol-A diglycidyl ether (DGEBA), but with longer chains to provide more flexibility in the material (Fig. 3.5). DGEBA is already used in literature to develop vitrimers [51–53], which is also applied for 3D printing.[13, 15, 54]
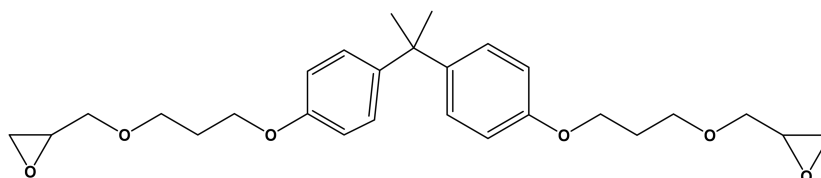
Figure 3.5: Chemical structure of bisphenol-A propoxylate diglycidyl ether.

A simplified illustration of the reversible bond exchange reactions within the dynamic covalent network at elevated temperatures is shown in Figure 3.6.
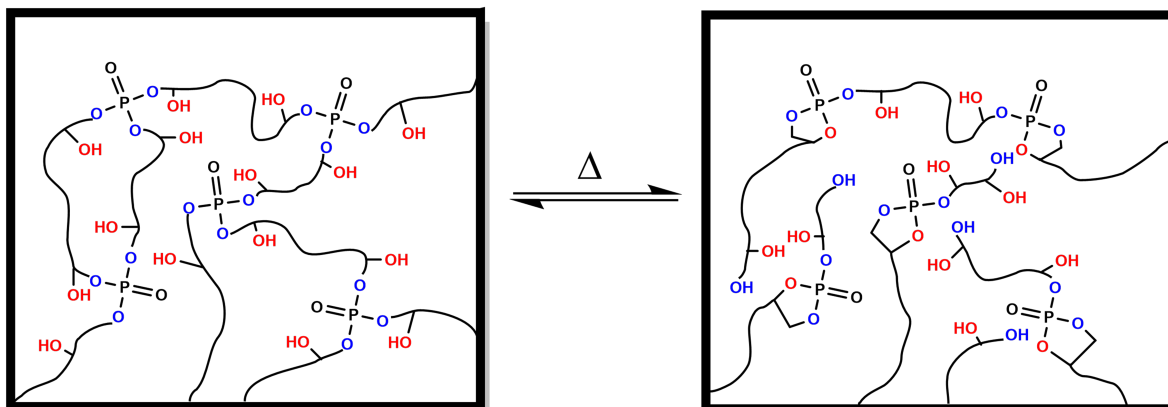
Figure 3.6: A simplified illustration of the reversible bond exchange reactions within the network.

In order to synthesize a DCN with this chemistry, this reaction needs to be investigated. Fortunately, Penczek's group has researched this synthesis in detail over the years, in which important points that need to be considered are discussed below:

1. The reaction of epoxide groups with P-OH groups is catalyzed by acidic protons, hence the reaction stops once all the P-OH groups are consumed. With the addition of a catalyst, the reaction proceeds by the homopolymerization of the epoxide groups with the free alcohol group forming an ether bond (Fig. 3.7). [44]
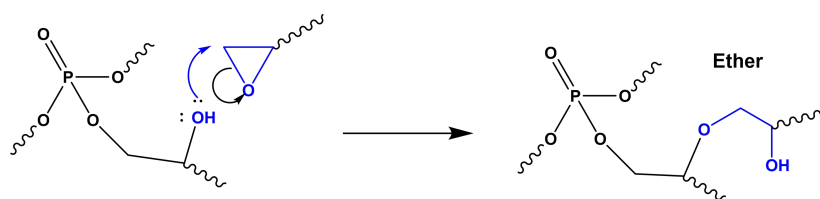
Figure 3.7: Reaction mechanism of the ether formation of neighboring β-hydroxyl group with an epoxide group.

2. The ratio of phosphoric acid influences the conversion to mono-, di- and triesters. The research performed by Penczek *et al.* [55] shows that higher concentration of phosphoric acid, increases the conversion to monoesters.

3. The reactivity of the consumption of a P-OH group increases over time, i.e. the reaction kinetics increases from mono, di- to triesters ($k'_2 > k'_1 > k'_0$). The reason is due to the hydrogen bonding of the neighboring β-hydroxyl groups, enhances the reactivity of the P-OH group (Fig. 3.8).[56]
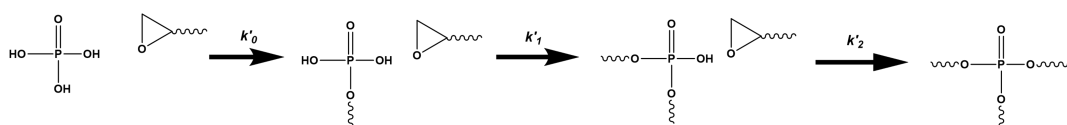
Figure 3.8: A scheme of the reaction steps towards phosphate triesters. Redrawn from [45].

Given these reactivity features, the homopolymerization of the monomer described in the first point needs to be suppressed in order to obtain a high concentration of neighboring β-hydroxyl groups. According to literature, the phosphate formation is highly temperature dependent. Since, complete consumption of P-OH groups is achieved within minutes at 100 °C, the side products can be sufficiently avoided.[44] Finally, the high conversion to triesters is crucial, given their enhanced reactivity and crosslink density compared to mono- and diesters.[57]

3.2 Materials & methods

3.2.1 Materials

Bisphenol-A propoxylate diglycidyl ether (>= 99 % purity) was obtained from Sigma Aldrich. Phosphoric acid crystals (>99 % purity) was obtained from ThermoFisher Chemicals. Tetrahydrofuran (THF) was obtained from Biosolve. All compounds were used as is, without further drying.

3.2.2 Material characterization

Nuclear Magnetic Resonance (NMR)

Proton (H^1), carbon (^{13}C) and phosphorous (^{31}P) nuclear magnetic resonance (NMR) spectroscopy were performed in a Bruker 400 MHz Bruker Avance III spectrometer at 25 °C.

Variable temperature ^{31}Phosphorous solid state NMR (VT ^{31}PSSNMR)

Variable temperature (VT) ^{31}P solid-state NMR (SSNMR) measurements were performed under static conditions, without magic angle spinning, using a one pulse sequence with a 90 °pulse of 5 µm and an inter-scan delay of 10 seconds. A 0.0485 M triphenylphosphate (TPhP) solution in CDCl$_3$ was used as a chemical shift reference at 17.70 ppm. Two variable temperature experiment cycles were performed, a heating cycle from 60 °C to 120 °C at intervals of 20 °C, and a cooling cycle in reverse order. The system was allowed to stabilize until equilibrium was reached at 60 °C, as well as for 15 min at each temperature.

Within the network, a dynamic equilibrium exists between two states: the ring-opened phosphate state, which signifies the chain extension link with an adjacent β-hydroxyl group, and the ring-closed state, representing the dissociated state of the chains in which the neighboring β-hydroxyl has reacted with the phosphate (Fig. 3.4). The dissociation rate of the crosslink depends on the concentration of the ring-opened state with a neighboring β-hydroxyl functionality ([OP]), while the association relies on the concentration of the ring-closed state ([CP]) and the free -OH groups from the dissociated polymer chains ([-OH]). Hence, the equilibrium constant K is represented as such:

$$K = \frac{[CP] \cdot [-OH]}{[OP]} \tag{3.1}$$

A 1:1 stoichiometry in the synthesization assumes that the network will contain dissociated phosphate esters and polymer -OH functionalities in a 1 to 1 ratio. Moreover, the OH content in the network remains the same, because both association and dissociation processes are a transesterification reaction. Based on this, the concentration ratio between the dissociated and associated phosphate esters can be determined from the VT ^{31}PSSNMR spectra by calculating the areas of the corresponding peaks. Additionally, employing Gibbs' fundamental equation and Van 't Hoff's law allows for the determination of the $\Delta H°$ for the dissociation process through the temperature dependence of [CP]/[OP].

$$\Delta G° = \Delta H° - T \Delta S° = -RT \ln K \tag{3.2}$$

$$\ln K = \frac{-\Delta H°}{RT} + \frac{\Delta S°}{R} \tag{3.3}$$

$$\ln\left(\frac{[CP]}{[OP]}\right) = \frac{-\Delta H°}{RT} + \frac{\Delta S°}{R} - \ln[-OH] \tag{3.4}$$

Fourier transform - infrared spectroscopy (FT-IR)

FT-IR were recorded on a PerkinElmer Spectrum Two at room temperature with a spectral width between 4000 cm^{-1} and 400 cm^{-1}.

Size Exclusion Chromatography (SEC)

Size Exclusion Chromatography (SEC) was taken with the Shimadzu Prominence-I LC-2030C 3D. The used eluent was THF with a flow rate of 1 mL/min at 40 °C. Polystyrene standards purchased from Agilent were used for calibration.

Gel fraction

The gel fractions were determined by weighing a sample (m_i) in a vial and let it swell for 72 hours in dry THF. After which, the solvent is removed and the sample is washed with fresh dry THF and dried in a vacuum oven overnight at 110 °C. The dried sample was weighed (m_d) and the gel fraction was calculated as follows:

$$gel\,fraction = \frac{m_d}{m_i} * 100\%$$ (3.5)

3.2.3 Thermal Characterization

Differential scanning calorimetry (DSC)

DSC measurements were conducted using a TA Intruments DSC Q2000. 2 - 5 mg of material was heated and cooled between -50 and 200 °C in two cycles with a heating rate of 10 and 40 °C/min. As reference, an empty pan was used.

Thermogravimetric Analysis (TGA)

Temperature ramp and isothermal experiments were performed with the TA instruments TGA Q500 machine. For the former, samples (5 - 10 mg) were heated under nitrogen flow (60 mL/min) from room temperature to 100 °C and kept isothermal for 30 min at 100 °C to dry out the sample, following a temperature increase with 10 °C/min until 800 °C was reached. For the latter, the temperature was rapidly increased from room temperature to 100 °C with 20 °C/min and kept isothermal for 30 min. Once more, the temperature increased with 20 °C/min until 180 or 200 °C was reached and kept isothermal for 120 min.

Dynamic mechanical thermal analysis (DMTA)

Dynamic Mechanical Thermal Analysis (DMTA) was performed on rectangular shaped compression molded samples using film tension setup in a DMA Discovery 850 (TA instruments). Temperature ramp was performed from -50 °C to 200 °C at 3 °C/min under 1 % oscillatory strain and a frequency of 1 Hz. A preload force of 0.001 N and a force track of 110 % was used. The storage and the loss modulus were recorded as a function of temperature.

3.2.4 Rheology

All rheology experiments were measured using the Discovery HR-20 (TA instruments) on a 8 mm parallel stainless steel plate geometry. Experiments were performed with an axial force of 1 or 4.5 ± 0.1 N.

Oscillatory time sweep experiments

Oscillatory time sweep experiments were performed before each stress relaxation experiment at 200 °C for 15 min under 1 % oscillatory strain and at an angular frequency of 1 Hz to erase any thermal history of each sample. The temperature is than slowly lowered to the desired temperature of the experiment.

Stress relaxation

There are several ways to model the viscoelastic behavior of a material. The Maxwell model is the most simple model for describing stress-relaxation tests. If a constant strain is applied on this model, the stress immediately increases to a maximum value and exponentially decays to zero depending on both the stiffness and the intrinsic viscosity of the material. The time it takes for the stress within the material relaxes is given by the characteristic relaxation time (τ), which is written as the ratio between the viscosity and the modulus ($\tau = \eta/G_0$).

Stress relaxation experiments were conducted across a range of temperatures to determine the temperature-dependent viscoelastic response of the material. The relaxation modulus $G(t)$ is plotted versus the step time under a constant strain of 5 % and normalized to $G(t)$ at t = 1 s, ($G(1s)$), in order to compare the relaxation rates solely based on the kinetics of bond exchange. However, the analysis of stress relaxation curves show a non-exponential behavior of the network, indicating that the curves were not to be fitted with the Maxwell model but with a stretched exponential function as depicted in the equation below [58]:

$$\frac{G(t)}{G(1s)} = \frac{\exp\left(-\left(\frac{t}{\tau}\right)^{\beta}\right)}{\exp\left(-\left(\frac{1}{\tau}\right)^{\beta}\right)} \tag{3.6}$$

Where β is the stretching parameter ranging between 0 and 1, characterizes the distribution of relaxation times, in which $\beta = 1$ corresponds to a mono-exponential decay, while lower values indicate a contribution of other relaxation modes that do not describe the relaxation profile well. [59]

Moreover, the viscosity of the sample can be calculated by multiplying the normalized stress relaxation with the apparent plateau modulus (G_0), from the following equation:

$$\eta = G_0 \cdot \tau \tag{3.7}$$

Considering this, an Arrhenius relationship between the viscosity and the reaction kinetics is found, seen in the equation below:

$$ln(\eta) = ln(\eta_0) + \frac{E_a}{RT} \tag{3.8}$$

Where η_0 is the characteristic viscosity, R is the gas constant, T the temperature. The viscosities of the corresponding temperature can be plotted and the slope can be used to determine the flow activation energy (E_a) of the system.

Frequency sweep

Frequency sweep experiments from 10^{-2} or 10^{-3} rad/s to 100 rad/s were performed on the network between 160 and 200 °C. The oscillation amplitude was set to 1 % strain. The storage modulus, loss modulus and tan(δ) were followed as a function of the frequency.

Flow temperature ramp

Flow temperature ramp experiments were performed from 80 °C or 130 °C to 200 °C with 2.0 °C/min. An axial force of 1.0 ± 0.1 N and 5 kPa of stress was used in order to determine the viscosity change with increasing temperature.

3.2.5 Reprocessing via extrusion

Reprocessing of the material was performed in an Xplore micro-compounder MC 15 HT with a twin screw setup. Approximately 15 g of the material was grinded and loaded at 120 °C and 200 °C into the extruder. The torque was measured from 160 °C to 200 °C at a screw speed of 1 RPM. The extrusion was performed at 200 °C, through a 1.75 mm nozzle and a nitrogen flow was used for purging the barrel.

3.3 Synthesis

For the network formation, 20.95 g (45.9 mmol) of BAPDGE and 4 ml THF were placed in a 100 ml round-bottom flask. 3 g (30.6 mmol) phosphoric acid was dissolved in 3.5 ml dry THF in a separate vial. In the meantime, the oil bath was heated to 110 °C, which is well above the boiling temperature of THF (66 °C).[60] The reaction was started, by adding the dissolved phosphoric acid to the flask with BAPDGE at room temperature, after which the mixture was immediately placed in the hot oil bath under argon flow to react and let the THF evaporate out. A network was formed after 2 minutes and was kept under argon flow for 30 minutes before being removed from the oil bath and transferred to a vacuum oven, where it was dried at 120 °C for 24 hours to form an amorphous polymer network.

Figure 3.9 shows a phosphorus (^{31}P) solid-state nuclear magentic resonance (SSNMR) spectrum at 60 °C, where a broad peak at 0.9 ppm, which is indicative of phosphate di- and triesters,

and a smaller peak observed at 17.4 ppm corresponds to the dissociated cyclic intermediate state.[61] The [31]PSSNMR was taken at 60 °C, since the network lacks dynamicity at lower temperatures to acquire a NMR spectrum with a slightly higher resolution.
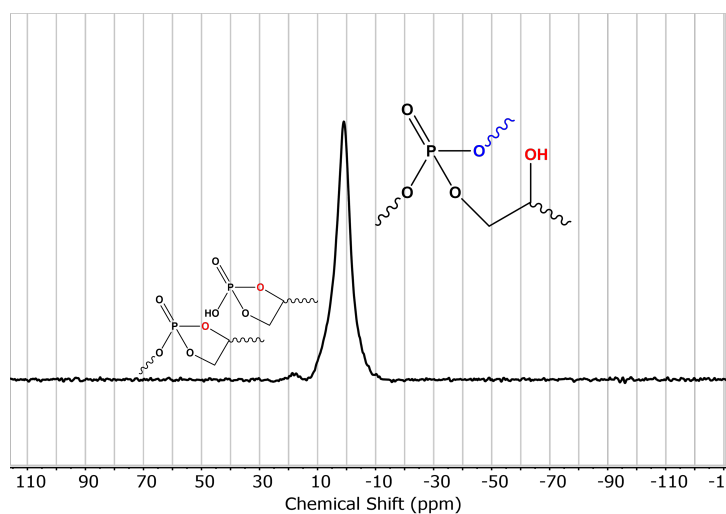
Figure 3.9: The [31]PSSNMR spectrum at 60 °C of the network. The small peak (17.4 ppm) corresponds to the cyclic intermediate state, and the bigger peak (0.9 ppm) the ring-opened state.

4

Results & Discussion

A dynamic covalent network (DCN) was synthesized by reacting a trifunctional phosphoric acid crosslinker with the bi-functional bisphenol-A propoxylate diglycidyl ether (BAPDGE) within minutes. FT-IR analysis revealed the reduction of the epoxide peak at 907 cm^{-1} and the appearance of a P-OC bond at 1006 cm^{-1} (Fig. 4.1).[62, 63] However, the stretching of the epoxide and the P-OC bond are both identified at 826 cm^{-1}, suggesting that complete conversion had not been achieved.[62, 64] This observation is further supported by a gel fraction of 70 %. The synthesized network was reprocessed into rectangular shapes of approximately 24 mm by 16 mm by compression molding under 100 bar at 130°C for 1 hour. Subsequently, the network was slowly cooled to 80°C under the same pressure, followed by active cooling to room temperature and a gel fraction of 70 % was obtained. From the rectangular molded shapes, rectangular bars of approximately 8 mm in width and 0.8 mm in thickness, were cut and circular disks with a diameter of 8 mm were punctured, which were used for DMTA and rheology experiments.
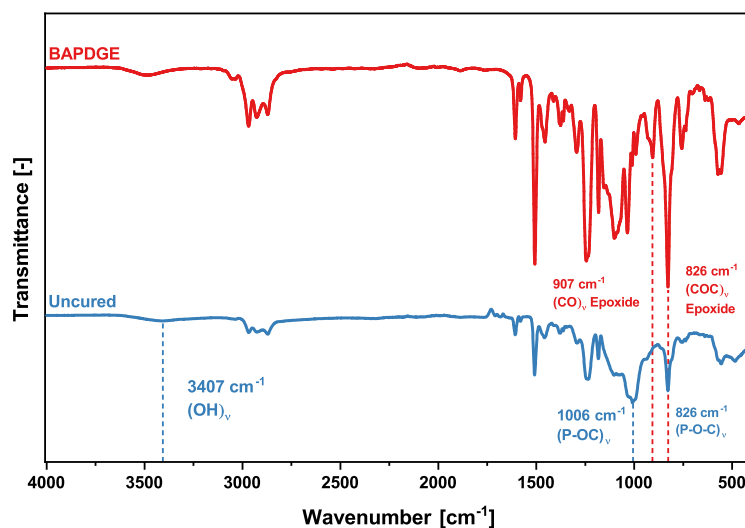
Figure 4.1: FTIR spectra of BAPDGE and the uncured network.

4.1   Characterization

4.1.1   Exchange mechanism determination

The exchange mechanism of the network was analyzed by varying the temperature within the [31]PSSNMR spectroscopy from 60 to 120 °C. The heating and the cooling cycles are represented in Figure 4.2, whereby upon heating both peaks, corresponding to the ring-closed state (around 17 ppm) and ring-opened state (around 1 ppm), increase in height. However, by quantifying the area under each peak, it becomes evident that the area corresponding to the ring-closed peak increase, while the area of the ring-opened state decrease (Table 4.1). This indicates that the ring-opened state dissociates to the ring-closed state, which is more stable at higher temperature.

Table 4.1: Ratios between [OP] and [CP] during heating and cooling cycles of VT [31]PSSNMR, all normalized at [CP].

Temperature [°C]	Heating cycle		Cooling cycle	
	[CP]	[OP]	[CP]	[OP]
60	1	99	-	-
80	1	35	1	12
100	1	11	1	7.2
120	1	5.7	1	5.7

Utilizing Equation 3.4, the reaction enthalpy towards the dissociated state equals $53 \pm 3 \, \text{kJ/mol}$ from the slope of Figure 4.3. Compared to the PCL-based phosphate ester network developed by Majumdar *et al.*,[43] this network exhibits a significantly higher dissociation enthalpy, suggesting that the dissociated state is less stabilized. Hence, the equilibrium shift towards the dissociated state is more temperature dependent.

Furthermore, a shift is visible of the ring-open state from approximately 0.9 ppm to -0.6 ppm. By looking at both peaks, despite an increase in height, they become narrower, due to the improved resolution at higher temperatures. This phenomenon may also account for the shift towards lower ppm values, as it is expected that the peak is located in the negative ppm range.[61]

Finally, the cooling cycle visualizes the reversibility of the network in which the concentration of the dissociated cyclic intermediate state reduced and the phosphate ester peak increased accordingly. Since equilibration times are higher in the cooling cycles and equilibrium was not yet reached, the areas of the peaks are not the same as of the heating cycle, thus, the reaction enthalpy in the cooling ramp is not considered (Fig. 4.2).
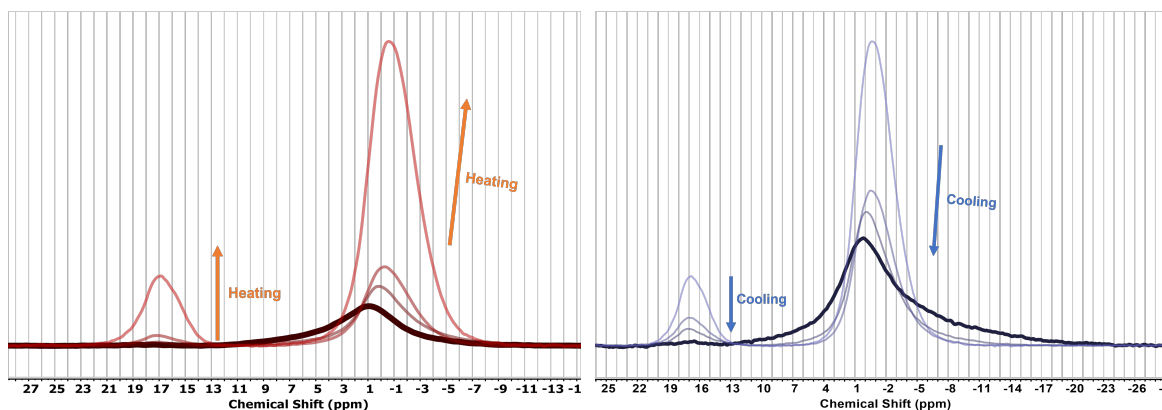
Figure 4.2: The heating/cooling cycle from 60 °C to 120 °C with 15 min equilibration at each temperature.
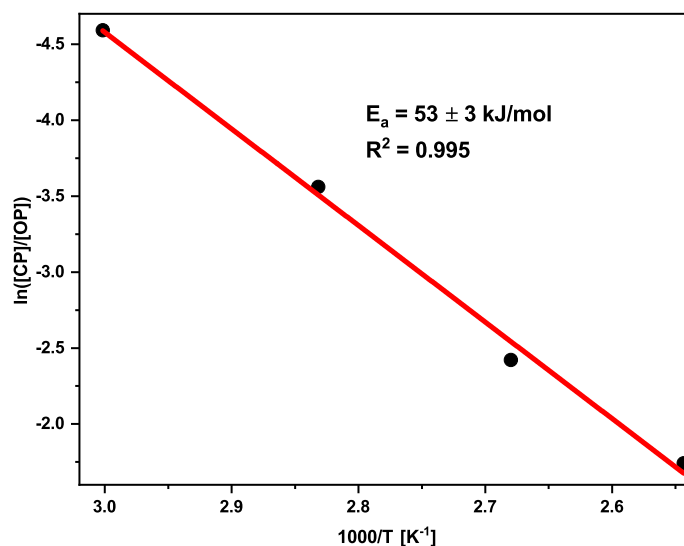
Figure 4.3: Temperature dependence of the ratio between cyclic phosphate esters and ring-opened phosphate esters.

4.1.2 Rheology

Stress relaxation

Stress relaxation experiments were performed with different samples at 140 °C, 160 °C, 180 °C and 200 °C under 5 % strain for 1 hour, results of which are shown in Figure 4.4. The stress relaxation profiles show a complete relaxation within an hour for temperatures above 160 °C. Moreover, as the temperature increases, complete relaxation occurs earlier, as depicted in Table 4.2. The stress relaxation times were determined by fitting the stress relaxation profiles using Equation 3.6 at different temperatures. From the unnormalized stress relaxation profiles, the G_0 was obtained by fitting it with Equation C.1, represented in Table C.1.

Subsequently, Equation 3.7 was used to calculate the viscosities (Table 4.2). Finally, the temperature dependence of the stress relaxation as obtained from the fit is represented in an Arrhenius plot, from which the flow activation energy (E_a) is found to be 101 ± 10 kJ/mol (Fig. 4.4). Notably, the values of the stress parameter β decrease significantly with increasing temperature, due to possible ether formation of the unreacted epoxides that are more dominant at elevated temperatures. Nevertheless, the stress relaxation times indicate a rapid relaxation ranging from approximately 143 to 5 seconds, as well as the low viscosity values at 180 °C and 200 °C.
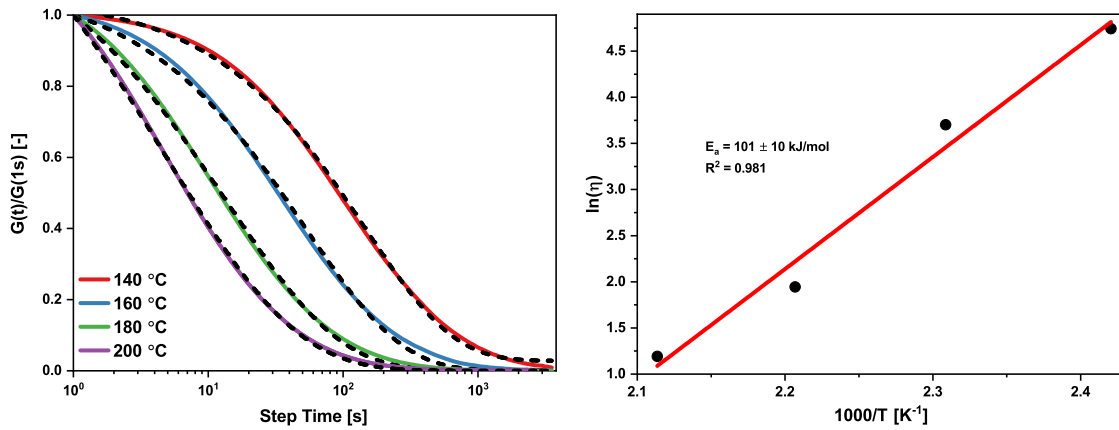
Figure 4.4: The stress relaxation profiles of distinct samples at different temperatures (left). The Arrhenius plot from the viscosities at each temperature (right).

Table 4.2: The quantitative values from the fitted data of the stress relaxation curves from Figure 4.4.

Temperature [°C]	τ[s]	β	η [MPa·s]
140	142.8	0.66	114.8
160	52.2	0.60	40.5
180	13.6	0.51	7.0
200	4.8	0.44	3.3

Frequency sweep

To obtain a better understanding of the viscoelastic behavior of the network, frequency sweep experiments were performed with three different samples at 160 °C, 180 °C and 200 °C under oscillatory shear to gather data on the bond exchange effects under different angular frequencies (Fig. 4.5). First noticeable at higher frequencies, is the decrease in the plateau storage modulus from 0.63 to 0.4 MPa. As expected because at higher temperatures, the equilibrium shifts towards the dissociated state, hence a lower plateau modulus is observed. Towards lower frequencies, the viscous component is more dominant, seen by the increase and decrease of the loss and storage modulus. The onset of the drop in the storage modulus moves to higher

frequencies with increasing temperatures, indicating an increase in the bond exchange rate. Finally, with increasing temperatures the crossover points to full viscous behavior move towards higher frequencies confirming again its faster bond rearrangements, namely from 0.006 rad/s at 160 °C, 0.017 rad/s at 180 °C to 0.021 rad/s at 200 °C.
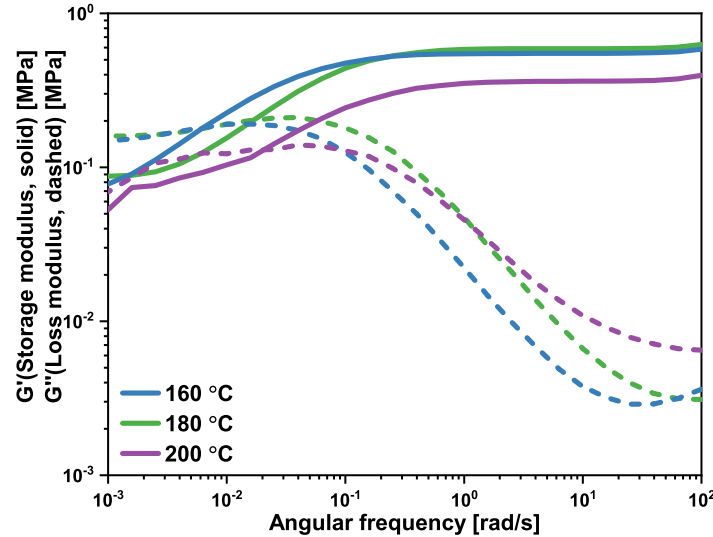
Figure 4.5: Frequency sweep experiments of the uncured network at different temperatures on different samples.

4.1.3 Thermal characterization

Thermogravimetric analysis (TGA) determined that 5 % of the network degraded around 271 °C (Fig. B.3). The thermo-mechanical properties of the network were analyzed with dynamic mechanical thermal analysis (DMTA), results of which are shown in Figure 4.6. A significant drop in storage modulus, attributed to the glass transition (T_g), is observed around 33 °C. This observation is consistent with the T_g value of 32 °C measured by the DSC (Fig. B.1). Following the rubbery plateau with a plateau modulus of approximately 3 MPa, a subsequent drop in the storage modulus is observed at around 120 °C. This is indicative of a dissociative network, since the crosslink density decreases at higher temperature due to the shift towards the dissociated state. However, the storage modulus increases above 150 °C, which may be assigned to further curing of the network. The reason for this could be due to the incomplete conversion, in which unreacted epoxides may interact with available hydroxyl groups. At higher temperatures, the concentration of free -OH groups increases, leading to the formation of permanent crosslinks.
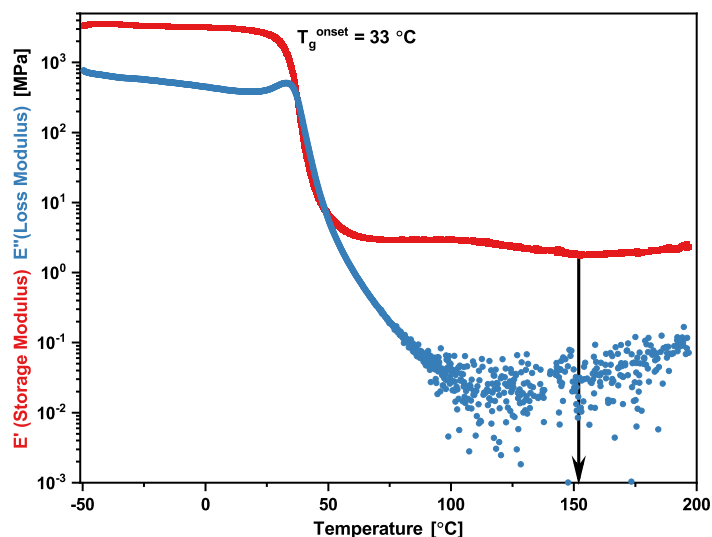
Figure 4.6: The temperature sweep experiment on a rectangular shaped sample in which an elongated force is applied and the moduli are followed.

4.2   Cured network

Instead of a drying process at 120 °C, the network was cured in the vacuum oven at 180 °C for 24 hours and taken out after cooling it to 80 °C. The ^{31}P-NMR shows that the equilibrium of the network at room temperature shifted to the dissociated cyclic phosphate intermediate, due to the increased curing temperature (Fig. A.5). The FT-IR spectra in Figure 4.7 show an increased intensity of the peak corresponding to stretching of the ether and P=O groups at 1101 cm^{-1} relative to the P-OC peak at 1006 cm^{-1}, confirming the increase of homopolymerization of the remaining epoxide groups.[64] Furthermore, the gel fraction increased from 70 % to approximately 98 %, indicating an increase of network formation. The enhanced crosslink density limits molecular motion, leading to an observed increase in the T_g measured at 43 °C using DSC (Fig. B.2).

Nevertheless, the network was still reprocessable by compression molding with the same procedure as described in section 4, but now, it was performed at 150 °C. Subsequently, thermal and mechanical analyses were performed on the cured network.
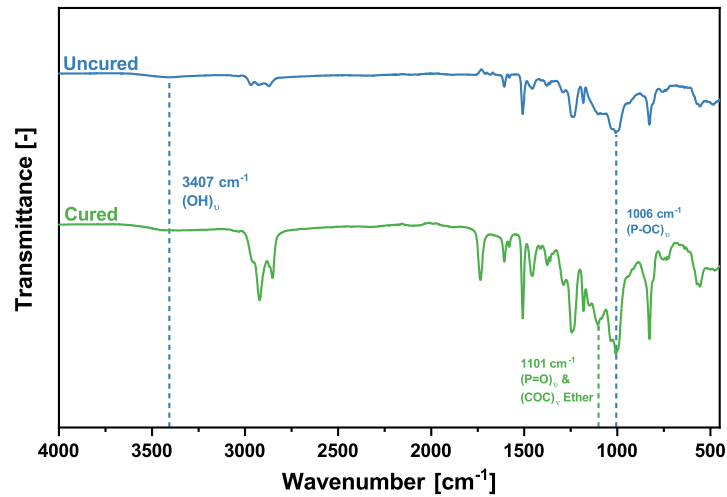
Figure 4.7: FTIR spectra of the uncured and cured network.

4.2.1 Rheology

Stress relaxation

The study involved performing stress relaxation experiments in shear on different samples over a range of temperatures (140-200 °C). The stress relaxation profiles of the cured network shown in Figure 4.8 indicate not only a slower relaxation, but also not complete relaxation within one hour. Further analysis, by creating an Arrhenius plot, indicates an E_a of 66 ± 7 kJ/mol, which is lower than the uncured sample (Fig. 4.8). By looking at Table C.1, the uncured network is more temperature responsive than the cured network, noticed by the decrease of G_0 with increasing temperature as opposed to the relatively constant G_0 of the cured network. The results show that the flow activation energy is highly dependent on the architecture of the network.

Furthermore, at 180 °C and 200 °C, the relaxation profiles display an early flattening at the end, which presumes that residual stress is present within the sample due to the permanent crosslinks. Table C.1 provides the G_0, from which the viscosities are calculated with Equation 3.7 (Table 4.3). The viscosity increased in comparison to the uncured network, indicating that the cured network does not flow easily, ultimately concluding that the cured network is unsuitable for 3D printing.
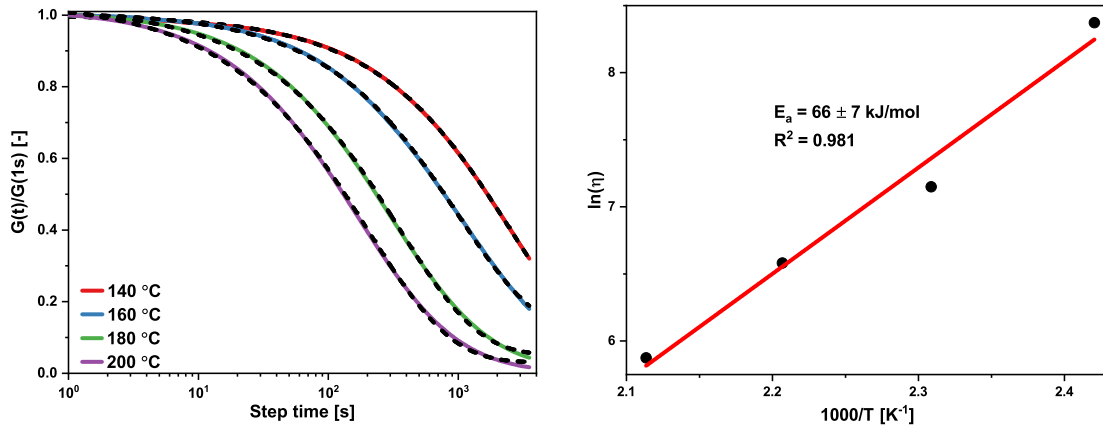
Figure 4.8: The stress relaxation profiles of different samples at different temperatures (left). The Arrhenius plot from the viscosities at each temperature (right).

Table 4.3: The quantitative values from the fitted data of the stress relaxation curves from Figure 4.8.

Temperature [°C]	τ[s]	β	η [MPa·s]
140	2536	0.71	4329
160	995.7	0.72	1274
180	345.6	0.70	722.0
200	114.0	0.71	356.0

Frequency sweep

Frequency sweep experiments were conducted at 160 °C, 180 °C, and 200 °C on one sample (Fig. 4.9). Upon comparison with the uncured network, the crossover is not identified at similar frequencies, coupled with a less significant drop in the storage modulus towards lower frequencies, suggesting a further crosslinked network. Additionally, at higher angular frequencies and temperatures, a decrease in plateau storage modulus from 3.4 MPa at 160 °C to 2.7 MPa at 200 °C was observed, indicative of a dissociative network. At last, the onset of the drop in storage modulus shifted towards higher frequencies with increasing temperatures, signifying an increase in the exchange rate at elevated temperatures.
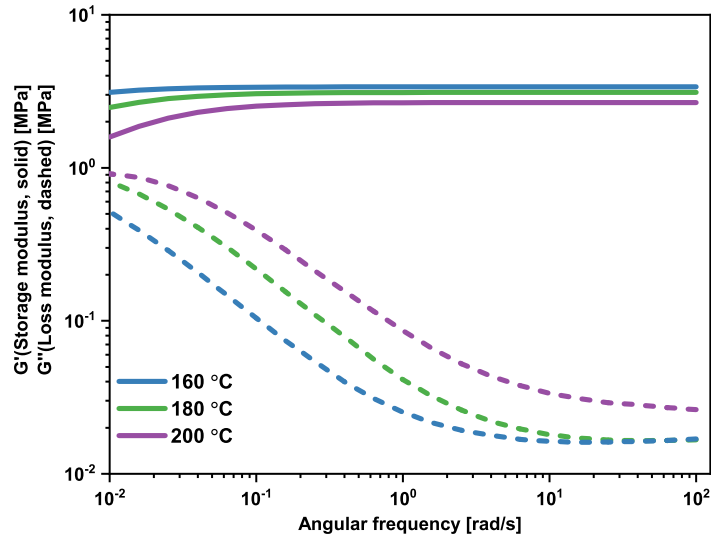
Figure 4.9: Frequency sweep experiment of the cured network at different temperatures on one sample with increasing temperature.

4.2.2 Thermal characterization

The DMTA results, represented in Figure 4.10, show an increase in T_g to 47 °C, which is consistent with the DSC results (Fig. B.2). The drop towards the rubbery plateau as opposed to the uncured network is less. Additionally, the storage modulus exhibits an increase of approximately 7 MPa in the plateau modulus. Notably, no significant drop in the storage modulus is observed, confirming the reduced dynamicity within the network (Fig. 4.10). Finally, the TGA analysis determined that the temperature at which 5 % of the network degraded was at 290 °C (Fig. B.3).
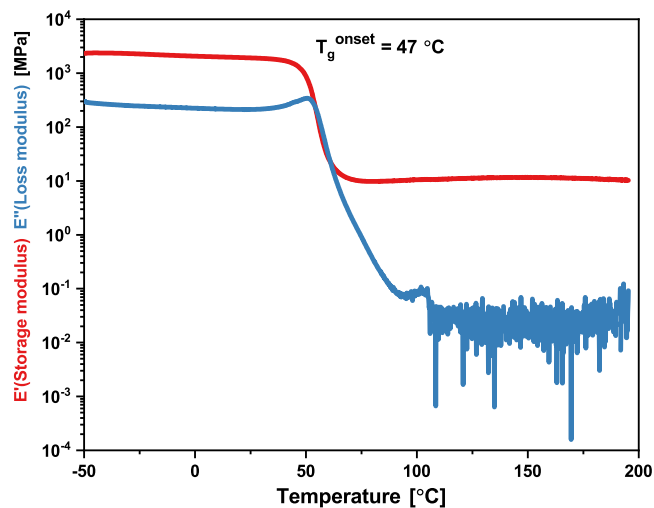
Figure 4.10: The temperature sweep experiment on a rectangular shaped sample in which an elongated force is applied and the moduli are followed.

4.3   Extrusion

The processability of the network was investigated by extruding the uncured network. The uncured network was grinded in smaller particles and added in the extruder at an initial temperature of 120 °C. The extruder had a difficult task to rotate the screws at 1 RPM below the maximum torque limit of 40 Nm. Consequently, the temperature was increased in steps of 20 °C until the torque remained constant, which was achieved at 160 °C after at least 35 min in the extruder. Once the torque was constant, the network was a homogeneous viscous material (Fig. 4.11). As the temperature increased, a noticeable decrease in torque is observed, with the torque measuring 28 Nm at 200 °C. Ultimately, after 50 min, the network flowed out of the extruder and a filament was visible in Figure 4.11 on the right including a video. The video shows that the filament maintained its shape and did not break. However, as the filament remained in the extruder for a longer period, it obtained a yellow hue. The yellow hue is indicative of the curing process of the network, thus, a reduction of the dynamic properties, which resulted in small cracks visible in the filament (Fig. E.1).
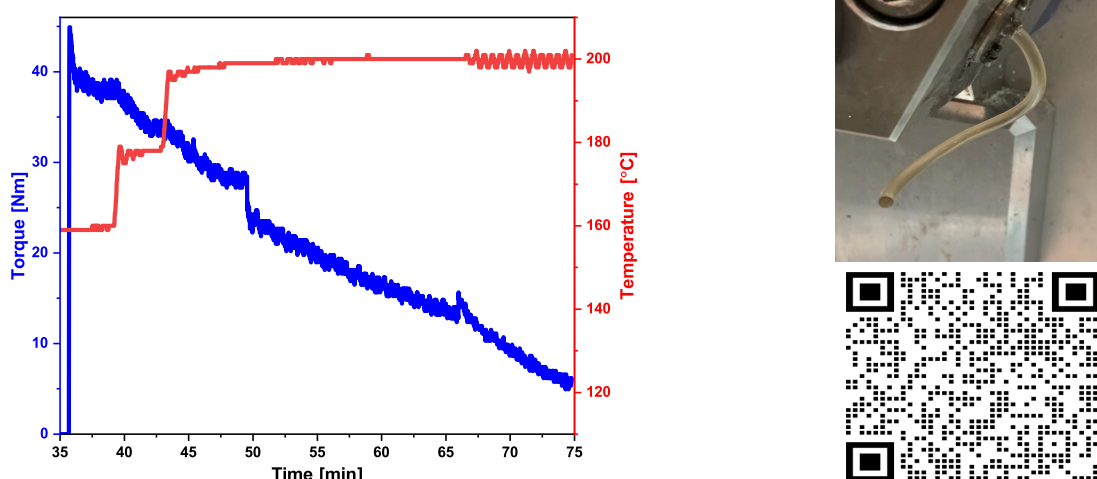
Figure 4.11: The torque declines with increasing temperature. At 50 min the network is extruded and the torque drops further down (left). An image of the extrudate with the QR code to the corresponding video (right).

Subsequently, the extrudates were reprocessable by compression molding and stress relaxation experiments were conducted for comparison to the neat network (Fig. 4.12). The stress relaxation times have increased after extrusion (Table E.1).

In addition, the hydrolytic stability of the extrudates was examined over a period of 23 days. The extrudates retained its shape for the first 9 days; however, after 16 days, it lost its structure and transformed into a mushy consistency (Fig. E.3). Moreover, the extrudates exhibited stability in THF for at least 24 hours, indicating their resilience in both water and THF environments (Fig. E.4).
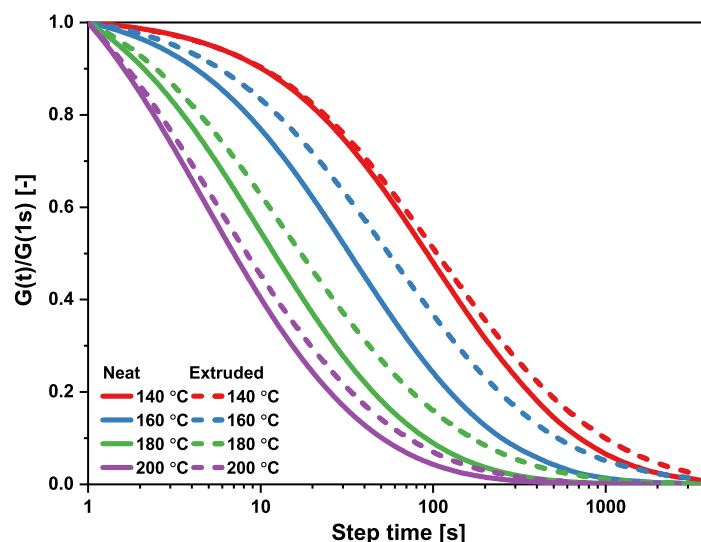
Figure 4.12: Stress relaxation profiles of the neat uncured network and the uncured network after extrusion on different samples with increasing temperature.

An attempt was made to investigate the reprocessability of multiple extrusion cycles at 200 °C. The torque reached its limit above 40 Nm multiple times at 1 RPM, but after 25 min, the network turned into a viscous state and the torque remained below its limit. Subsequently, after 55 min, the torque remained constant and was extruded (Fig. 4.13). Notably, the torque remained higher compared to the previous extrusion attempt. This increase in torque can be attributed to the longer residence time in the extruder above its curing temperature, which subsequently reduces the flowability of the network (Fig. 4.13).

Subsequently, a second cycle of extrusion was performed, however, the network degraded to such an extent that the extrudates turned black (Fig. E.2). According to the TGA, only 3 % degradation at of an isothermal experiment at 200 ° was observed (Fig. B.4). The reason of the accelerated degradation within the extruder can be attributed to both the mechanical mixing of the network as well as the absence of a nitrogen environment.
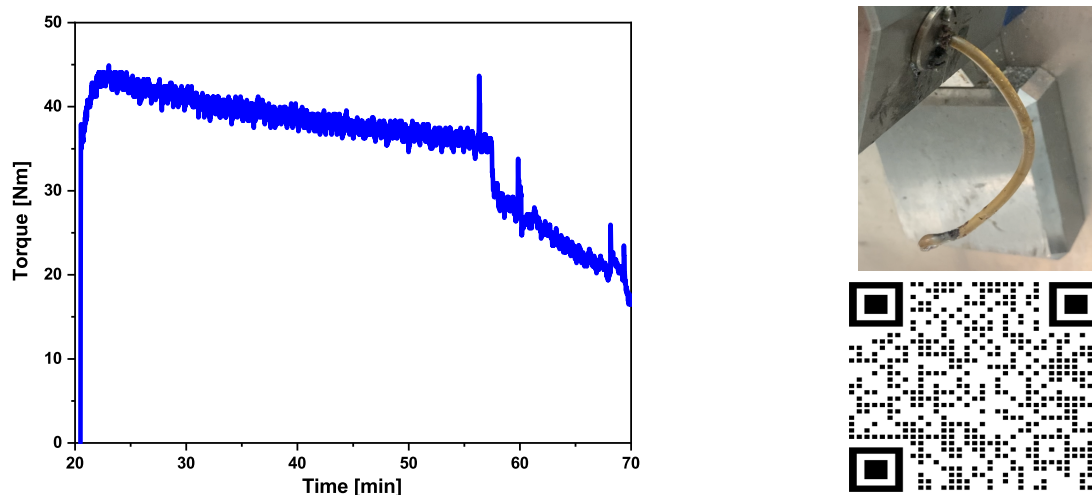
Figure 4.13: The torque stabilized after 55 min at 200 °C, until the network is extruded and the torque drops (left). An image of the extrudate with the QR code to the corresponding video (right).

Lastly, the flow properties of the network for FDM were determined with a flow temperature ramp experiment (Fig. 4.14). Noticeably, the viscosity decreases linearly with increasing temperature, until 180 °C is reached and the viscosity increases. Ideally, a significant drop in viscosity at a certain temperature is observed, which indicates the transition from elastic behavior to viscous flow behavior. The absence of viscous flow behavior, has a negative impact on the reprocessability and mechanical properties of the material, thus, making it challenging to 3D print it with FDM.
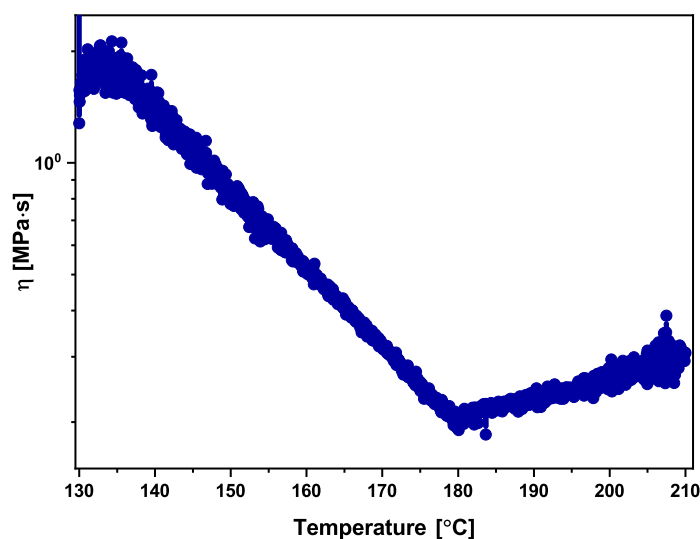
Figure 4.14: The viscosity versus the temperature profile of an uncured sample after a flow temperature experiment.

5

Conclusion

This study aimed at developing a printable dynamic covalent network (DCN) suitable with fused deposition modeling. A phosphate ester based DCN was synthesized within minutes by reacting phosphoric acid crystals with a diglycidyl ether. This reaction resulted in the formation of pendent hydroxyl groups through epoxide ring-opening, enabling neighboring group assisted rearrangements without the aid of a catalyst.

The kinetics of bond rearrangements were analyzed using variable temperature ^{31}PSSNMR, revealing the reversibility of the transition between the ring-closed and ring-opened states during heating and cooling cycles. The reaction enthalpy for the dissociation process was determined to be 53 kJ/mol, indicating that the exchange reaction has a higher activation barrier than the phosphate network described by Majumdar.[43]

Stress relaxation experiments conducted on the network revealed rapid bond rearrangements, with the fastest relaxation time of approximately 5 seconds at 200 °C. Additionally, the viscosities at 180 °C and 200 °C were low. Moreover, frequency sweep experiments demonstrated an earlier onset of viscous behavior at higher frequencies as the temperature increased, indicating the potential printability of the network. However, from the DMTA results, it can be observed that a curing process occurs at temperatures above 150 °C. This leads to a notable reduction in bond rearrangement kinetics, as well as an elevation in the viscosity and modulus. Consequently, it can be concluded that the curing of the network must be avoided during the extrusion process.

Nevertheless, it was possible to extrude a homogeneous filament at 200 °C with an extrusion speed of 1 RPM. However, it should be noted that the network requires a minimum residence time of 55 minutes at 200 °C to exhibit viscous behavior, which is not ideal considering the increase of the modulus and viscosity shown by the flow temperature experiment. Furthermore, the bond exchange reactions slow down and small cracks within the extrudate become present with a more yellow hue. Nevertheless, stress relaxation experiments show a slight increase in the stress relaxation times after extrusion. Unfortunately, no further analysis and optimization of the network's extrusion process has been conducted due to time restrictions.

6

Outlook

An alternative approach for extruding this network would involve initially starting the temperature below the curing temperature to obtain a more viscous material, followed by rapidly raising the temperature to a suitable level, such as 180 °C, where the viscosity is low enough to promote smooth extrusion. Additionally, conducting recyclability experiments to assess the reprocessability of the material is crucial for investigating its overall lifespan. However, producing a filament suitable for FDM printing poses a challenge, due to the lack of viscous flow within the network that would prevent successful extrusion. Consequently, a new synthesis approach is necessary to reduce the crosslink density of the network.

The usual approach to decrease the crosslink density is to add a chain extender, such as a dimer fatty acid (DFA), which had been already performed in literature.[13, 65] However, the attempts on synthesizing with a chain extender were unsuccessful in obtaining the desired network. The methods attempted are detailed in appendix D, wherein it is observed that the resulting network exhibited similarities to the cured network, despite a reduction of the T_g due to the DFA acting as a plasticizer. While this approach holds potential, the numerous unsuccessful trials and time constraints shifted the focus towards another synthesis route.

Fortunately, an alternative approach had successfully resulted in an improved DCN. The synthesis is based on points 2 and 3 in section 3.1, whereby a reverse addition method was employed. The addition allowed for the initial formation of monoesters, followed by subsequent conversion to diesters and ultimately triesters, resulting in a network. Additionally, the ratio of the diglycidyl ether and phosphoric acid was optimized to promote the formation of longer chains. Moreover, the type of solvent was also adjusted because the more apolar the solvent, the more reactive the phosphoric acid was due to less hydrogen bonds with the solvent.[44]

This optimized synthesis formed a network with a lower crosslink density, resulting in a lower viscosity at lower temperatures as opposed to the uncured network. However, it should be noted that the following synthesis, found in appendix F, had only formed a network once on a small scale. Despite repeated attempts, the synthesis had failed consistently. Notably, the occurrence of phase separation of a network at the top and an epoxide resin beneath it. Various

modifications, including changing the flask volume, solvent ratios, addition rates had been investigated, yet none had successfully helped to form a complete network. Nevertheless, a flow temperature ramp, represented in Figure 6.1, shows a significant drop in viscosity at around 160 °C. The viscosity is significantly lower as opposed to the uncured original network (Fig. 4.14), suggesting its potential for FDM printing. Moreover, in appendix F, stress relaxation experiments are shown, but these results were considered insufficient.
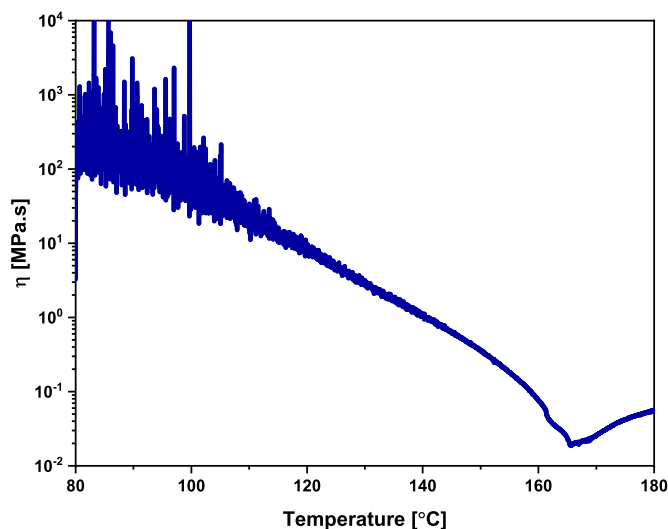
Figure 6.1: The viscosity versus the temperature profile of the optimized network sample from a flow temperature ramp experiment.

Alternatively, the utilization of another kind of diglycidyl ether that has a higher molecular weight could resolve the current problems as well. For example, reacting poly(Bisphenol A-co-epichlorohydrin), glycidyl end-capped (Sigma-Aldrich, 25036-25-3, M_n ~1075) with phosphoric acid should obtain a less dense dynamic covalent network due to the increased chain length (Fig. 6.2). A successful attempt on synthesizing the network with the same procedure as in section 3.3 was made, however, the network was not reprocessable via compression molding. Nevertheless, it would be interesting to further study and optimize this network.
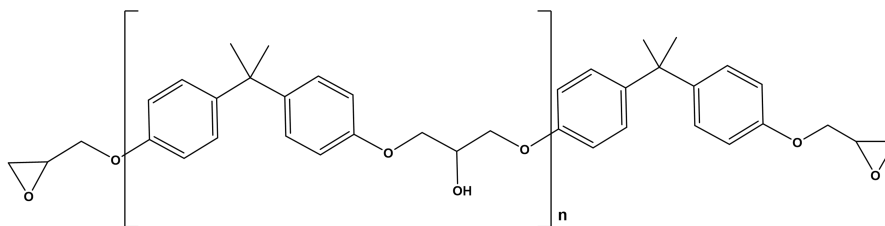
Figure 6.2: The chemical structure of poly(Bisphenol A-co-epichlorohydrin), glycidyl end-capped.

The advantage of the network presented in this work is that no catalysts are present within the system that can leach out over time. However, the use of catalysts do improve the kinetics

of bond exchange reactions, resulting in a potentially significantly improved and extrudable network. Further research is needed to experiment with the most effective catalysts. Generally catalysts that promote transesterification should be sufficient, e.g. Zinc acetate $(Zn(ac)_2)$,[13] triazabicyclo[4.4.0]dec-5-ene (TBD) [66] and 1,8-diazabicyclo[5.4.0]undec-7-ene (DBU).[67]

References

1 Ambrosi, A., & Pumera, M. (2016). 3D-printing technologies for electrochemical applications. *Chemical Society Reviews*, *45*(10), 2740–2755. https://doi.org/10.1039/c5cs00714c

2 Ngo, T. D., Kashani, A., Imbalzano, G., Nguyen, K. T., & Hui, D. (2018). Additive manufacturing (3d printing): A review of materials, methods, applications and challenges. *Composites Part B: Engineering*, *143*, 172–196.

3 What is additive manufacturing? [Accessed at 23 February 2023]. (2017). https://www.energy.gov/eere/articles/what-additive-manufacturing#1

4 Hull, C. W. (1986). Apparatus for production of three-dimensional objects by stereolithography [US Patent 4,575,330]. https://doi.org/10.1088/1757-899X/716/1/012012

5 Siemiński, P. (2021). Chapter 7 Introduction to fused deposition modeling. In *Additive manufacturing* (pp. 217–275). https://doi.org/10.1016/B978-0-12-818411-0.00008-2

6 Cesarano, J., & Calvert, P. D. (2000). Freeforming Objects with Low-binder Slurry [US Patent 6,027,326].

7 Beaman, J. J., & Deckard, C. R. (1990). Selective laser sintering with assisted powder handling [US Patent 4,938,816].

8 The evolution of the 3d printing materials market in 2019: Polymers [Accessed on 16 February 2023]. (2019). https://facfox.com/docs/kb/the-evolution-of-the-3d-printing-materials-market-in-2019-polymers

9 Javaid, M., Haleem, A., Pratap, R., Suman, R., & Rab, S. (2021). Role of additive manufacturing applications towards environmental sustainability. *Advanced Industrial and Engineering Polymer Research*, *4*(4), 312–322. https://doi.org/10.1016/j.aiepr.2021.07.005

10 Truby, R. L., & Lewis, J. A. (2016). Printing soft matter in three dimensions. *Nature*, *540*, 371–378. https://doi.org/10.1038/nature21003

11 Zuo, H., Liu, Z., Zhang, L., Liu, G., Ouyang, X., Guan, Q., Wu, Q., & You, Z. (2021). Self-healing materials enable free-standing seamless large-scale 3d printing. *Science China Materials*, *64*(7), 1791–1800. https://doi.org/https://doi.org/10.1007/s40843-020-1603-y

12 Markforged. (n.d.). 3D Printing Setting Impacting Part Strength [Accessed on 08-06-2023]. https://markforged.com/resources/learn/design-for-additive-manufacturing-plastics-composites/understanding-3d-printing-strength/3d-printing-settings-impacting-part-strength

13 Shi, Q., Yu, K., Kuang, X., Mu, X., Dunn, C. K., Dunn, M. L., Wang, T., & Qi, H. J. (2017). Recyclable 3d printing of vitrimer epoxy. *Materials horizons*, *4*(4), 598–607. https://doi.org/10.1039/c7mh00043j

14 Appuhamillage, G. A., Reagan, J. C., Khorsandi, S., Davidson, J. R., Voit, W., & Smaldone, R. A. (2017). 3D printed remendable polylactic acid blends with uniform mechanical strength enabled by a dynamic Diels-Alder reaction. *Polymer Chemistry*, *8*(13), 2087–2092. https://doi.org/10.1039/c7py00310b

15 Casado, J., Konuray, O., Roig, A., Fernández-Francos, X., & Ramis, X. (2022). 3D printable hybrid acrylate-epoxy dynamic networks. *European Polymer Journal*, *173*(April). https://doi.org/10.1016/j.eurpolymj.2022.111256

16 Kloxin, C. J., & Bowman, C. N. (2013). Covalent adaptable networks: Smart, reconfigurable and responsive network systems. *Chemical Society Reviews*, *42*(17), 7161–7173. https://doi.org/10.1039/c3cs60046g

17 Craven James M. (1969). Cross-linked thermally reversible polymers produced from condensation polymers with pendant furan groups cross-linked with maleimides [US Patent 3,435,003].

18 Chen, X., Dam, M. A., Ono, K., Mal, A., Shen, H., Nutt, S. R., Sheran, K., & Wudl, F. (2002). A thermally re-mendable cross-linked polymeric material. *Science*, *295*(5560), 1698–1702. https://doi.org/10.1126/science.1065879

19 Scheutz, G. M., Lessard, J. J., Sims, M. B., & Sumerlin, B. S. (2019). Adaptable Crosslinks in Polymeric Materials : Resolving the Intersection of Thermoplastics and Thermosets. *Journal of the American Chemical Society*, *141*, 16181–16196. https://doi.org/10.1021/jacs.9b07922

20 Kristiawan, R. B., Imaduddin, F., Ariawan, D., Arifin, Z., et al. (2021). A review on the fused deposition modeling (fdm) 3d printing: Filament processing, materials, and printing parameters. *Open Engineering*, *11*(1), 639–649. https://doi.org/10.1515/eng-2021-0063

21 Sheoran, A. J., & Kumar, H. (2020). Fused deposition modeling process parameters optimization and effect on mechanical properties and part quality: Review and reflection on present research. *Materials Today: Proceedings*, *21*, 1659–1672. https://doi.org/10.1016/j.matpr.2019.11.296

22 Mohamed, O. A., Masood, S. H., & Bhowmik, J. L. (2015). Optimization of fused deposition modeling process parameters: A review of current research and future prospects. *Advances in manufacturing*, *3*(1), 42–53. https://doi.org/10.1007/s40436-014-0097-7

23 Jaster, L. (2016). Primary 3d printing processes [Accessed at 12 October 2022]. https://www.printspace3d.com/3d-printing-processes/

24 Kafle, A., Luis, E., Silwal, R., Pan, H. M., Shrestha, P. L., & Bastola, A. K. (2021). 3d/4d printing of polymers: Fused deposition modelling (fdm), selective laser sintering (sls), and stereolithography (sla). *Polymers*, *13*(18), 3101. https://doi.org/https://doi.org/10.3390/polym13183101

25 Fitzharris, E. R., Watanabe, N., Rosen, D. W., & Shofner, M. L. (2018). Effects of material properties on warpage in fused deposition modeling parts. *The International Journal of Advanced Manufacturing Technology*, *95*(5), 2059–2070. https://doi.org/https://doi.org/10.1007/s00170-017-1340-8

26 Rosli, A. A., Shuib, R. K., Ishak, K. M. K., Hamid, Z. A. A., Abdullah, M. K., & Rusli, A. (2020). Influence of bed temperature on warpage, shrinkage and density of various acrylonitrile butadiene styrene (abs) parts from fused deposition modelling (fdm). *AIP Conference Proceedings*, *2267*(1), 020072.

27 Davidson, J. R., Appuhamillage, G. A., Thompson, C. M., Voit, W., & Smaldone, R. A. (2016). Design Paradigm Utilizing Reversible Diels-Alder Reactions to Enhance the Mechanical Properties of 3D Printed Materials. *ACS Applied Materials and Interfaces*, *8*(26), 16961–16966. https://doi.org/10.1021/acsami.6b05118

28 Yang, K., Grant, J. C., Lamey, P., Joshi-imre, A., Lund, B. R., Smaldone, R. A., & Voit, W. (2017). Diels – Alder Reversible Thermoset 3D Printing : Isotropic Thermoset Polymers via Fused Filament Fabrication. *Advanced Functional Materials*, *27*, 1700317–1700328. https://doi.org/10.1002/adfm.201700318

29 Kim, S., Rahman, M. A., Arifuzzaman, M., Gilmer, D. B., Li, B., Wilt, J. K., Lara-Curzio, E., & Saito, T. (2022). Closed-loop additive manufacturing of upcycled commodity plastic through dynamic cross-linking. *Science Advances*, *8*, eabn6006. https://doi.org/10.1126/sciadv.abn6006

30 Niu, W., Zhang, Z., Chen, Q., Cao, P. F., & Advincula, R. C. (2021). Highly Recyclable, Mechanically Isotropic and Healable 3D-Printed Elastomers via Polyurea Vitrimers. *ACS Materials Letters*, *3*(8), 1095–1103. https://doi.org/10.1021/acsmaterialslett.1c00132

31 Joe, J., Shin, J., Choi, Y. S., Hwang, J. H., Kim, S. H., Han, J., Park, B., Lee, W., Park, S., Kim, Y. S., & Kim, D. G. (2021). A 4D Printable Shape Memory Vitrimer with Repairability and Recyclability through Network Architecture Tailoring from Commercial Poly(ϵ-caprolactone). *Advanced Science*, *8*(24), 1–11. https://doi.org/10.1002/advs.202103682

32 Choi, S., Park, B., Jo, S., Seo, J. H., Lee, W., Kim, D. G., Lee, K. B., Kim, Y. S., & Park, S. (2022). Weldable and Reprocessable Shape Memory Epoxy Vitrimer Enabled by Controlled Formulation for Extrusion-Based 4D Printing Applications. *Advanced Engineering Materials*, *24*(4), 1–10. https://doi.org/10.1002/adem.202101497

33 Roels, E., Terryn, S., Brancart, J., Verhelle, R., Assure, G. V., & Vanderborght, B. (2020). Additive Manufacturing for Self-Healing Soft Robots. *7*(6), 711–723. https://doi.org/10.1089/soro.2019.0081

34 Zheng, M., Guo, Q., Yin, X., Getangama, N. N., de Bruyn, J. R., Xiao, J., Bai, Y., Liu, M., & Yang, J. (2021). Direct ink writing of recyclable and in situ repairable photothermal polyurethane for sustainable 3d printing development. *Journal of Materials Chemistry A*, *9*, 6981–6992. https://doi.org/10.1039/d0ta11341g

35 Sun, S., Gan, X., Wang, Z., Fu, D., Pu, W., & Xia, H. (2020). Dynamic healable polyurethane for selective laser sintering. *Additive Manufacturing*, *33*, 101176. https://doi.org/10.1016/j.addma.2020.101176

36 Sun, S., Fei, G., Wang, X., Xie, M., Guo, Q., Fu, D., Wang, Z., Wang, H., Luo, G., & Xia, H. (2021). Covalent adaptable networks of polydimethylsiloxane elastomer for selective laser sintering 3D printing. *Chemical Engineering Journal*, *412*, 128675. https://doi.org/10.1016/j.cej.2021.128675

37 Robinson, L. L., Self, J. L., Fusi, A. D., Bates, M. W., Read De Alaniz, J., Hawker, C. J., Bates, C. M., & Sample, C. S. (2021). Chemical and Mechanical Tunability of 3D-Printed Dynamic Covalent Networks Based on Boronate Esters. *ACS Macro Letters*, *10*, 857–863. https://doi.org/10.1021/acsmacrolett.1c00257

38 Zhang, B., Kowsari, K., Serjouei, A., Dunn, M. L., & Ge, Q. (2018). Reprocessable thermosets for sustainable three-dimensional printing. *Nature Communications*, *9*. https://doi.org/10.1038/s41467-018-04292-8

39   Cui, C., An, L., Zhang, Z., Ji, M., Chen, K., Yang, Y., Su, Q., Wang, F., Cheng, Y., & Zhang, Y. (2022). Reconfigurable 4D Printing of Reprocessable and Mechanically Strong Polythiourethane Covalent Adaptable Networks. *Advanced Functional Materials*, *32*, 1–9. https://doi.org/10.1002/adfm.202203720

40   He, C., Shi, S., Wang, D., Helms, B. A., & Russell, T. P. (2019). Poly(oxime-ester) Vitrimers with Catalyst-Free Bond Exchange. *Journal of the American Chemical Society*, *141*, 13753–13757. https://doi.org/10.1021/jacs.9b06668

41   Zhang, H., Majumdar, S., Van Benthem, R. A., Sijbesma, R. P., & Heuts, J. P. (2020). Intramolecularly Catalyzed Dynamic Polyester Networks Using Neighboring Carboxylic and Sulfonic Acid Groups. *ACS Macro Letters*, *9*, 272–277. https://doi.org/10.1021/acsmacrolett.9b01023

42   Delahaye, M., Tanini, F., Holloway, J. O., Winne, J. M., & Du Prez, F. E. (2020). Double neighbouring group participation for ultrafast exchange in phthalate monoester networks. *Polymer Chemistry*, *11*(32), 5207–5215. https://doi.org/10.1039/d0py00681e

43   Majumdar, S., Mezari, B., Zhang, H., Van Aart, J., Van Benthem, R. A., Heuts, J. P., & Sijbesma, R. P. (2021). Efficient Exchange in a Bioinspired Dynamic Covalent Polymer Network via a Cyclic Phosphate Triester Intermediate. *Macromolecules*, *54*, 7955–7962. https://doi.org/10.1021/acs.macromol.1c01504

44   Penczek, S., Pretula, J., Kubisa, P., Kaluzynski, K., & Szymanski, R. (2015). Reactions of H3PO4 forming polymers. Apparently simple reactions leading to sophisticated structures and applications. *Progress in Polymer Science*, *45*, 44–70. https://doi.org/10.1016/j.progpolymsci.2015.01.001

45   Biela, T., Kubisa, P., & Penczek, S. (1992). Addition of oxiranes to the acids of phosphorus. Direction of ring opening. *193*, 1147–1164. https://doi.org/https://doi.org/10.1002/macp.1992.021930513

46   Jiao, C., Zhuo, J., Chen, X., Li, S., & Wang, H. (2013). Flame retardant epoxy resin based on bisphenol A epoxy resin modified by phosphoric acid. *Journal of Thermal Analysis and Calorimetry*, *114*(1), 253–259. https://doi.org/10.1007/s10973-012-2867-4

47   Iqra, A. R., Ayesha, A., Muhammad, F. S., & Asra, T. (2021). Multi-functional carbon fiber reinforced composites for fire retardant applications. *Key Engineering Materials*, *875 KEM*(February), 23–28. https://doi.org/10.4028/www.scientific.net/KEM.875.23

48   Huang, S. W., & Zhuo, R. X. (2008). Recent advances in polyphosphoester and polyphosphoramidate based biomaterials. *Phosphorus, Sulfur and Silicon and the Related Elements*, *183*(2-3), 340–348. https://doi.org/10.1080/10426500701734620

49   Tee, H. T., Lieberwirth, I., & Wurm, F. R. (2019). Aliphatic Long-Chain Polypyrophosphates as Biodegradable Polyethylene Mimics. *Macromolecules*, *52*(3), 1166–1172. https://doi.org/10.1021/acs.macromol.8b02474

50   Fang, L. F., Jeon, S., Kakihana, Y., ichi Kakehi, J., Zhu, B. K., Matsuyama, H., & Zhao, S. (2017). Improved antifouling properties of polyvinyl chloride blend membranes by novel phosphate based-zwitterionic polymer additive. *Journal of Membrane Science*, *528*, 326–335. https://doi.org/10.1016/j.memsci.2017.01.044

51   Kumar, A., & Connal, L. A. (2023). Biobased Transesterification Vitrimers. *Macromolecular Rapid Communications*, *2200892*, 1–21. https://doi.org/10.1002/marc.202200892

52 Altuna, F. I., Hoppe, C. E., & Williams, R. J. (2016). Shape memory epoxy vitrimers based on DGEBA crosslinked with dicarboxylic acids and their blends with citric acid. *RSC Advances*, *6*(91), 88647–88655. https://doi.org/10.1039/c6ra18010h

53 Manarin, E., Da Via, F., Rigatelli, B., Turri, S., & Griffini, G. (2022). Bio-Based Vitrimers from 2,5-Furandicarboxylic Acid as Repairable, Reusable, and Recyclable Epoxy Systems. *ACS Applied Polymer Materials*. https://doi.org/10.1021/acsapm.2c01774

54 Yuan, T., Zhang, L., Li, T., Tu, R., & Sodano, H. A. (2020). 3D Printing of a self-healing, high strength, and reprocessable thermoset. *Polymer Chemistry*, *11*(40), 6441–6452. https://doi.org/10.1039/d0py00819b

55 Penczek, S., Kaluzynski, K., & Pretula, J. (2007). Addition of H3PO4 to diglycidyl ethers of bisphenol A: Kinetics and product structure. *Journal of Applied Polymer Science*, *105*(1), 246–254. https://doi.org/10.1002/app.26087

56 Biela, T., Nyk, A., Kubisa, P., & Studies, M. (1992). Polyphosphate chains by Addition of Oxiranes to Phosphoric Acid. *Macromolecular chemistry, Macromolecular Symposia*, *60*, 155–163. https://doi.org/https://doi.org/10.1002/masy.19920600114

57 Kirby, A. J., & Nome, F. (2015). Fundamentals of Phosphate Transfer. *Accounts of Chemical Research*, *48*(7), 1806–1814. https://doi.org/10.1021/acs.accounts.5b00072

58 Lukichev, A. (2019). Physical meaning of the stretched exponential Kohlrausch function. *Physics Letters, Section A: General, Atomic and Solid State Physics*, *383*(24), 2983–2987. https://doi.org/10.1016/j.physleta.2019.06.029

59 Mauro, J. C., & Mauro, Y. Z. (2018). On the Prony series representation of stretched exponential relaxation. *Physica A: Statistical Mechanics and its Applications*, *506*, 75–87. https://doi.org/10.1016/j.physa.2018.04.047

60 American Chemical Society. (2015). Tetrahydrofuran [Accessed on 08-06-2023]. https://www.acs.org/molecule-of-the-week/archive/t/tetrahydrofuran.html

61 Procházková, E., Šimon, P., Straka, M., Filo, J., Májek, M., Cigáň, M., & Baszczyňski, O. (2021). Phosphate linkers with traceable cyclic intermediates for self-immolation detection and monitoring. *Chemical Communications*, *57*(2), 211–214. https://doi.org/10.1039/d0cc06928k

62 González, M. G., Cabanelas, J. C., & Baselga, J. (2012). Applications of FTIR on Epoxy Resins – Identification , Monitoring the Curing Process , Phase Separation and Water Uptake. https://doi.org/10.5772/36323

63 Merekenova, A. K., Boiko, G. I., Dergunov, S. A., Sarmurzina, R. G., Karabalin, U. S., & Lubchenko, N. P. (2018). A new monoalkyl phosphate ester based on a product derived from the recycling of a postconsumer polyethylene terephthalate waste. *Journal of Chemical Technology and Metallurgy*, *53*(1), 43–49.

64 Bardakçi, B., & Kaya, N. (2009). FT-IR spectroscopic study of triethyl phosphate adsorption on FAU type zeolite. *Asian Journal of Chemistry*, *21*(6), 4914–4918.

65 Zheng, M. (2021). *Study of Recyclable and Repairable Dynamic Covalent Polymers for Sustainable 3D Printing Development* (Vol. 7673). Electronic Thesis & Dissertation Repository. https://ir.lib.uwo.ca/etd/7673

66   Zhang, Y., Wang, H., Yang, S., & Huang, Z. (2022). Recyclable and High-Performance Thermosetting Polymers for Digital Light Processing 3D Printing. *2022 5th International Conference on Energy, Electrical and Power Engineering (CEEPE)*, 1–5. https://doi.org/10.1109/CEEPE55110.2022.9783401

67   Nifant'ev, I. E., Shlyakhtin, A. V., Tavtorkin, A. N., Kosarev, M. A., Gavrilov, D. E., Komarov, P. D., Ilyin, S. O., Karchevsky, S. G., & Ivchenko, P. V. (2019). Mechanistic study of transesterification in TBD-catalyzed ring-opening polymerization of methyl ethylene phosphate. *European Polymer Journal*, *118*, 393–403. https://doi.org/10.1016/j.eurpolymj.2019.06.015

Appendices

A Nuclear magnetic resonance
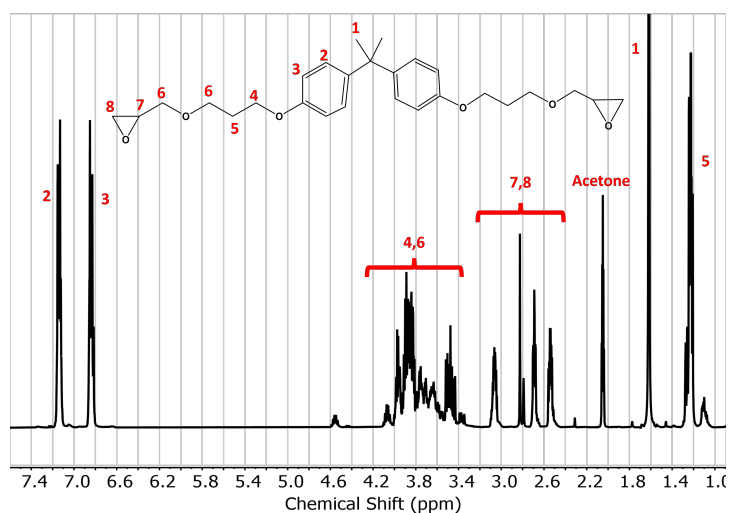
Figure A.1: NMR BAPDGE: ^{1}H-NMR (400 MHz, Acetone-d6) δ 7.61 (dq, J = 8.8, 2.4 Hz, 4H), 7.36 − 7.26 (m, 4H), 4.61 − 3.78 (m, 12H), 3.54 (dddt, J = 7.0, 5.7, 4.2, 2.8 Hz, 1H), 3.32 − 3.24 (m, 1H), 3.21 − 3.10 (m, 1H), 3.01 (qd, J = 5.4, 2.6 Hz, 1H), 2.09 (s, 6H), 1.81 − 1.64 (m, 6H).
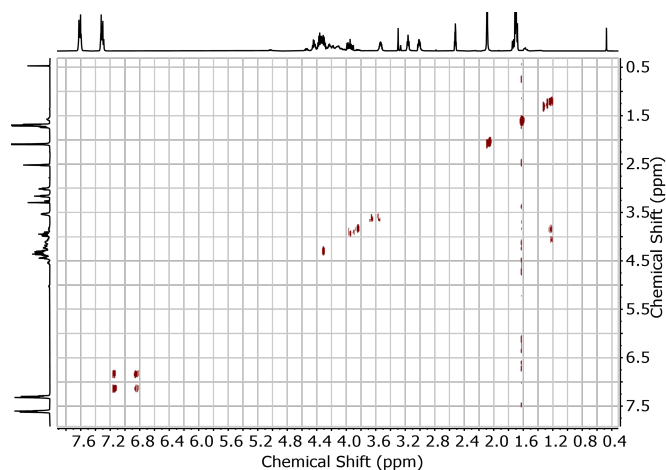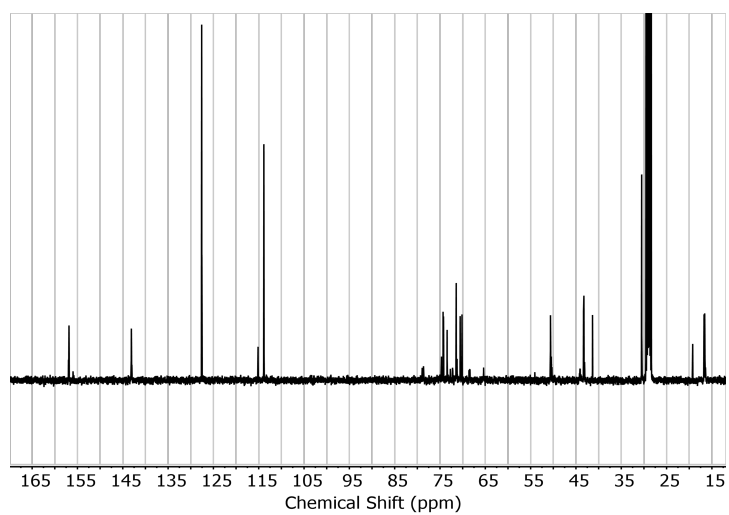

Figure A.2: 2D COSY (^{1}H/^{1}H) NMR of BAPDGE.

Figure A.3: ^{13}C-NMR (101 MHz, Acetone-d6) δ 156.87, 143.11, 127.57, 113.86, 74.32, 71.42, 70.15, 50.62, 43.25, 41.35, 30.50, 28.76.
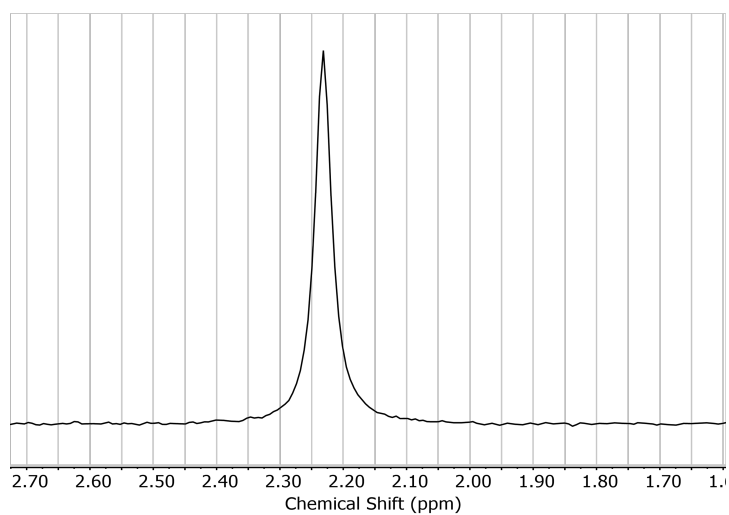
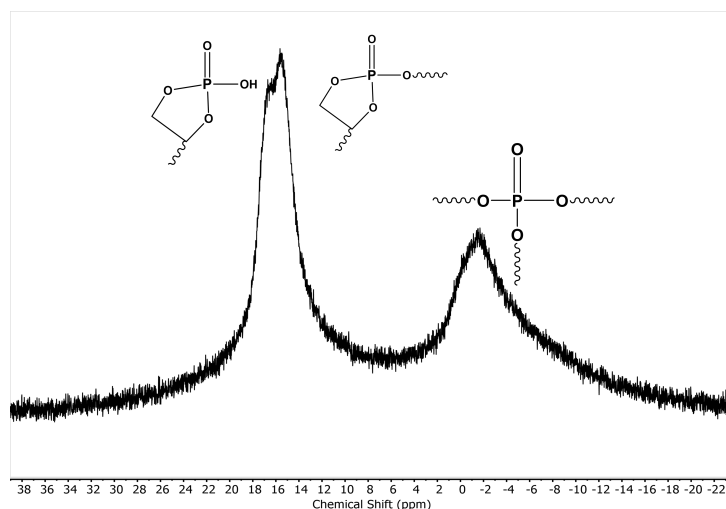Figure A.4: ^{31}P-NMR (162 MHz, Acetone-d6) δ 2.23.

Figure A.5: ^{31}P-NMR spectrum of the cured network in acetone-d6 performed at 25 °C, whereby the concentration of dissociated ring-closed state approximately 17 ppm is higher in comparison to the ring-opened state at -2 ppm.

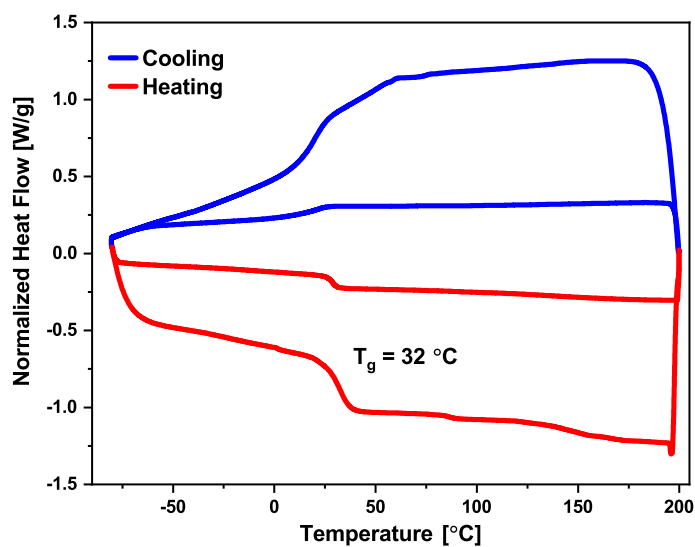# B   Thermal analysis

B.1   Differential scanning calorimetry

Figure B.1: DSC spectrum of the uncured network with two heating and cooling runs for the un-cured network (exo up). The heating and cooling rates were 10 °C/min and 40 °C/min
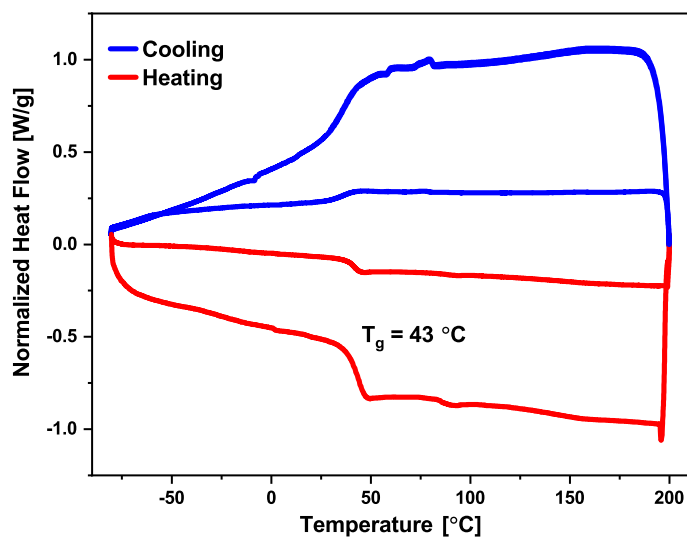
Figure B.2: DSC spectrum of the cured network with two heating and cooling runs for the uncured network (exo up).The heating and cooling rates were 10 °C/min and 40 °C/min
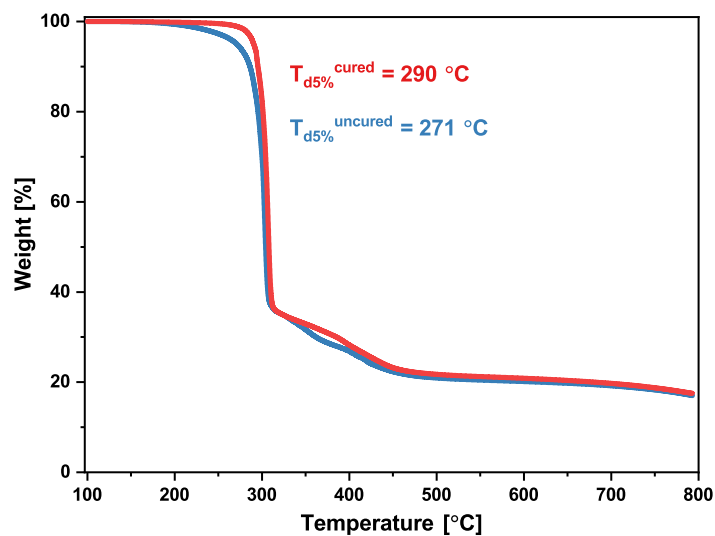
B.2   Thermogravimetric analysis

Figure B.3: TGA temperature sweep for uncured and cured network. The heating rate was 10 °C/min.
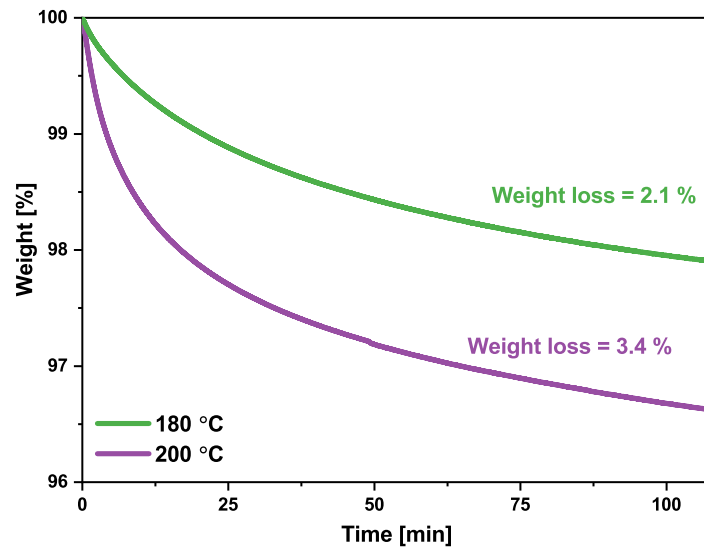
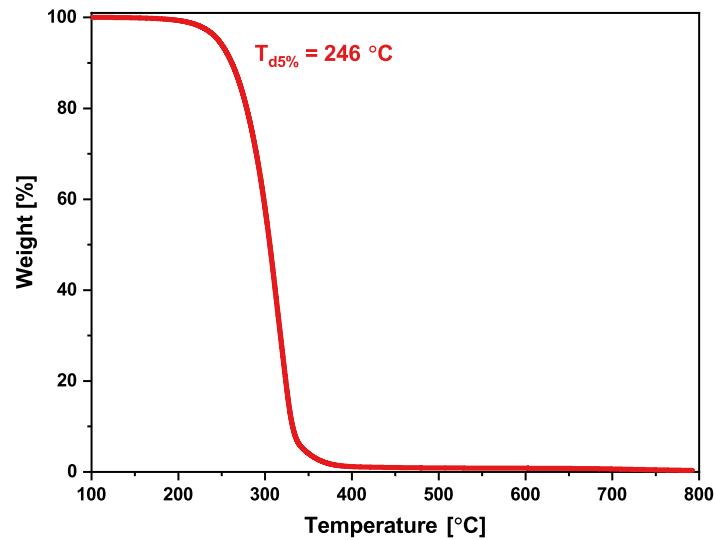Figure B.4: Isothermal TGA profiles of uncured network at 180 °C and 200 °C.

Figure B.5: TGA temperature sweep for BAPDGE. The heating rate was 10 °C/min.

C Plateau modulus determination

The G_0 is determined by fitting the storage modulus versus the step time of each stress relaxation profile with the stretched exponential equation:

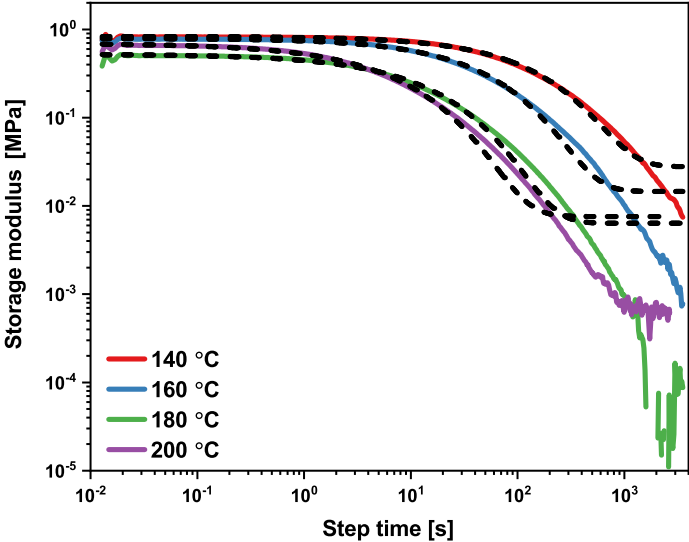$$G = G_0 e^{-(t/\tau)^\beta} + residual \tag{C.1}$$

Figure C.1: The storage modulus versus the step time to determine the G_0 of the uncured network.
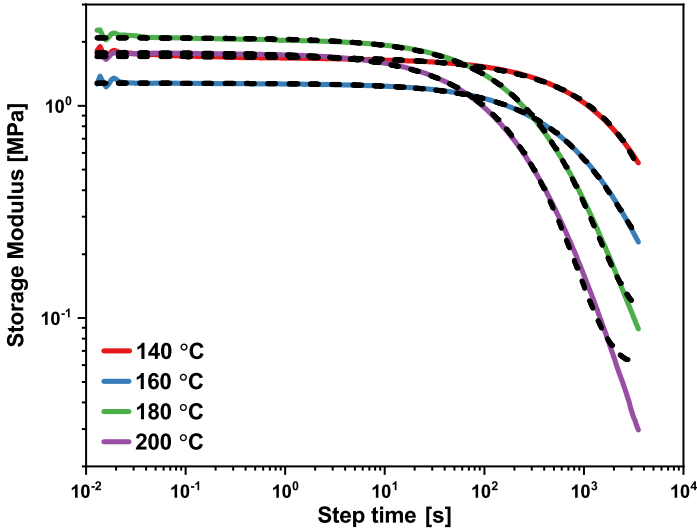

Figure C.2: The storage modulus versus the step time to determine the G_0 of the cured network.
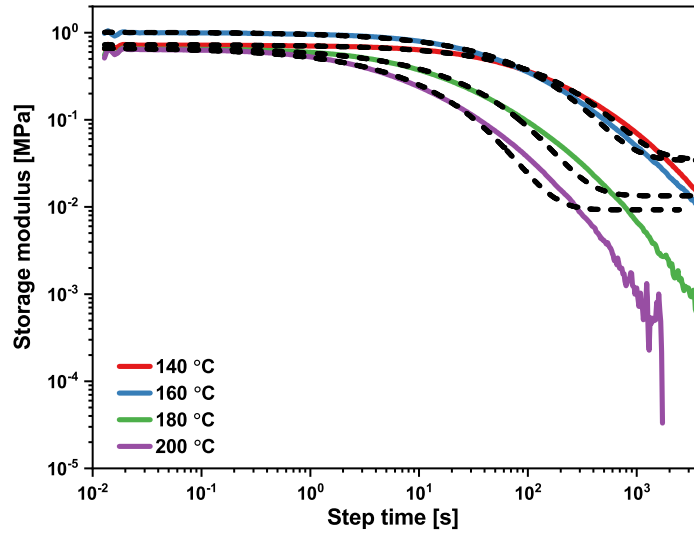
Figure C.3: The storage modulus versus the step time to determine the G_0 of the extruded network.

Table C.1: The G_0 from the fitted data of the unnormalized stress relaxation curves starting at 0.013 s.

Temperature [°C]	G_0Uncured [MPa]	G_0Cured [MPa]	G_0Extruded [MPa]
140	0.80	1.71	0.69
160	0.78	1.28	0.98
180	0.52	2.09	0.66
200	0.69	1.77	0.67

D Chain extension

Two synthesis methods were performed in order to react a dimer fatty acid (DFA) with BAPDGE as a chain extender to reduce the crosslink density. Phosphoric acid and DFA (Sigma-Aldrich,68783-41-5, hydrogenated C36, Mn~570 g/mol, ≤ 1.0 % trimer & ≤ 1.0 % mono) with a 1:0.75 ratio, were dissolved in dry THF. BAPDGE was weighed in a ratio of 1.5:1 to phosphoric acid and mixed with a bit of dry THF. Only after performing the same procedure as in section 3.3 and curing afterwards resulted in a network. This network showed similar properties as the cured network, only a reduction of the T_g (Fig. D.1). Indicating, that the DFA had not reacted but utilized as a plasticizer within the network.
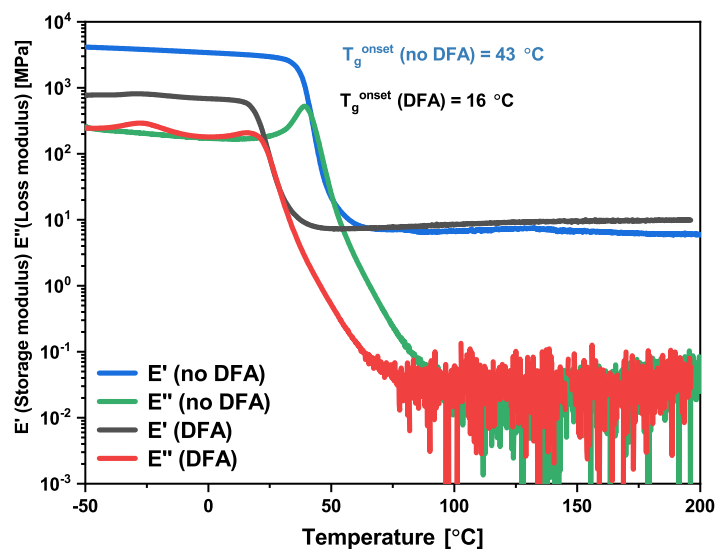
Figure D.1: DMTA spectra of the first iteration of the cured network and the cured network with DFA.

The second approach involved synthesizing chains of two DFA components and three BAPDGE components within each chain. The reaction was performed at 150 °C and monitored using size exclusion chromatography (SEC) to ensure the desired chain length was obtained. After reacting for 4 hours the desired chain length was obtained, according to the SEC (Fig. D.2). The reaction was immediately stopped by quenching it. Next, the system was heated to 110 °C and 10 mol% of phosphoric acid was added to crosslink the chains together or used as a catalyst for transesterification reaction of DFA and BAPDGE. Unfortunately, this method also failed, potentially due to side-reactions that resulted in a reduced concentration of OH groups within the system. Moreover, optimization in the ratios of the components could be investigated further.
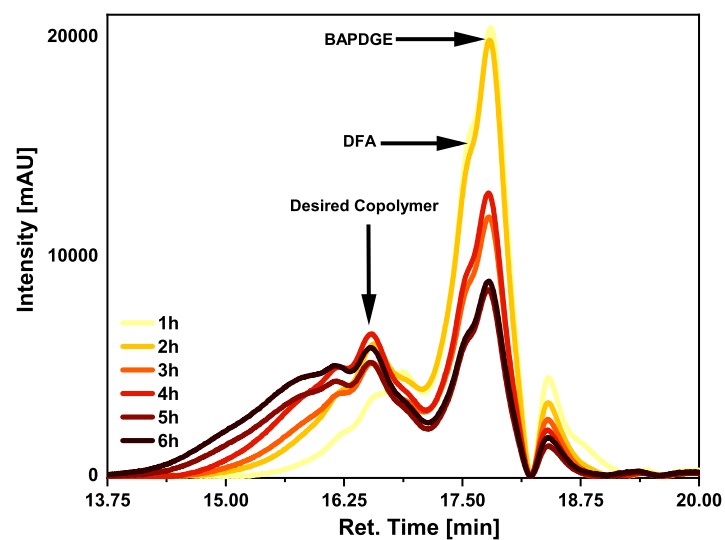
Figure D.2: SEC chromatogram of the synthesize of BAPDGE and DFA at different timescales. As the concentration of BAPDGE and DFA decrease, the concentration of various copolymers simultaneously increase.

E   Extrusion

Figure E.1: The extrudate turns more yellow and small cracks start to appear due to a longer residence time at 200 °C in the extruder.

Figure E.2: The extrudate burned after a longer residence time in which the network reduced in dynamic properties during a second extrusion cycle at 200 °C.

Stress relaxation

Table E.1: The quantitative values from the fitted data of the stress relaxation curves from Figure 4.12.

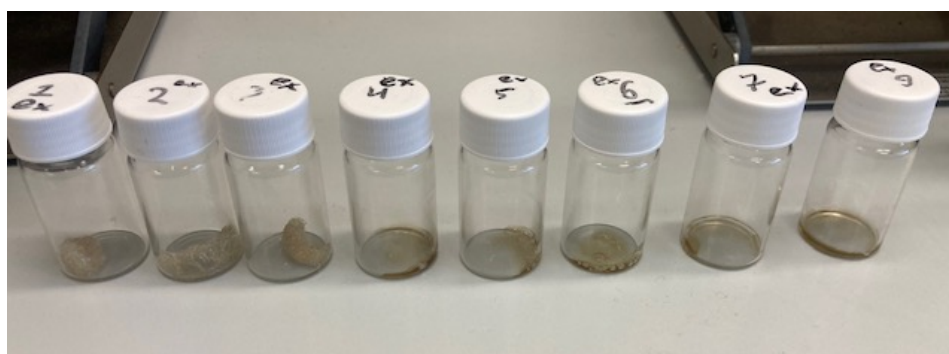| Temperature [°C]	τ[s]	β	η [MPa*s]
140	159.7	0.62	111.2
160	95.3	0.56	92.6
180	20.9	0.47	13.4
200	5.7	0.41	3.6

Solvent stability

Figure E.3: Dried samples after swollen in water for 23 days (from left to right).

Figure E.4: Extrudate swollen for 24 hours in THF.

F Potential optimized network

Synthesis

First, 345.8 mg (0.0035 mol) of phosphoric acid was dissolved in 2 ml dry 1,4 dioxane and 1736.5 mg (0.0038 mol) BAPDGE was dissolved in both 2 ml dry toluene and 7 ml dry 1,4-dioxane. The ratios of BAPDGE and phosphoric acid are 4:3 3/2. This ratio involves the formation of chains composed of 4 BAPDGE and 3 phosphoric acids, with the remaining 2/3 phosphoric acid was utilized as crosslinker to react with the remaining 2 epoxide groups to connect the chains. Whilst the dissolved phosphoric acid was placed into a 25 ml flask within the oil bath, the dissolved BAPDGE was placed in a dropping funnel under argon. Once the oil bath reached 100 °C, BAPDGE was added dropwise into the flask while stirring constantly. After complete addition of BAPDGE into the system, the temperature was raised to 120 °C, and the dropping funnel was replaced with a bubbler without oil to evaporate the solutions out of the system overnight. The next day, the formed network was washed with dry THF thrice and dried in a vacuum oven overnight at 120 °C.

Stress relaxation

Stress relaxation experiments were performed on different samples. However, no thermal curing for 15 min on 180 °C was performed, hence the thermal history of each sample is different, resulting in an insufficient stress relaxation experiment (Fig. F.1). Nevertheless, the network shows extremely fast relaxation at low temperatures, confirming the potential for further research in synthesizing this network consistently (Table F.1).
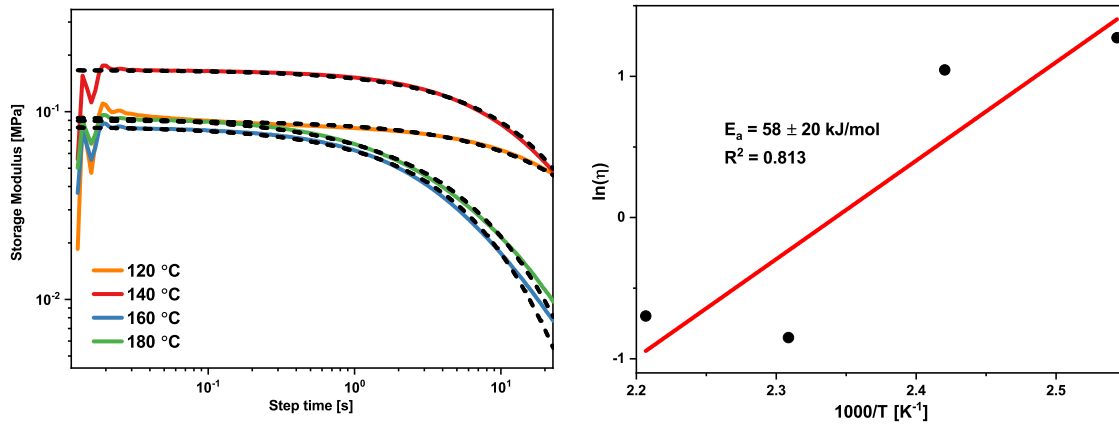
Figure F.1: Stress relaxation profiles of the optimized network on distinct samples with increasing temperature (left). The Arrhenius plot from the viscosities at each temperature (right).

Table F.1: The quantitative values from the fitted data of the unnormalized stress relaxation curves starting at 0.013 s from Figure F.1.

Temperature [°C]	τ [s]	β	G_0 [MPa]	η [MPa·s]
120	39.9	0.70	0.09	3.57
140	17.3	0.79	0.16	2.84
160	5.18	0.72	0.08	0.43
180	5.29	0.63	0.09	0.50